RICE UNIVERSITY

Carbon-Based Nanostructures as Advanced Contrast Agents for Magnetic Resonance Imaging

by

Jeyarama S. Ananta Narayanan

A THESIS SUBMITTED

IN PARTIAL FULFILLMENT OF THE

REQUIREMENTS FOR THE DEGREE

Doctor of Philosophy

APPROVED, THESIS COMMITTEE:

Lon J. Wilson, Professor and Chair

Chemistry

Robert H. Hauge, Distinguished Faculty

Chemistry

Enrique V. Barrera, Professor

Mechanical Engineering and Materials Science

HOUSTON, TEXAS

MAY, 2011

ABSTRACT

Carbon-Based Nanostructures as Advanced Contrast Agents for Magnetic Resonance Imaging

by

Jeyarama S. Ananta Narayanan

Superparamagnetic carbon-based nanostructures are presented as contrast agents (CAs) for advanced imaging applications such as cellular and molecular imaging using magnetic resonance imaging (MRI). Gadolinium-loaded, ultra-short single-walled carbon nanotubes (gadonanotubes; GNTs) are shown to have extremely high r_1 relaxivities (contrast enhancement efficacy), especially at low-magnetic field strengths. The inherent lipophilicity of GNTs provides them the ability to image cells at low magnetic field strength.

A carboxylated dextran-coated GNT (GadoDex) has been synthesized and proposed as a new biocompatible high-performance MRI CA. The r_1 relaxivity is ca. 20 times greater than for other paramagnetic Gd-based CAs. This enhanced relaxivity for GadoDex is due to the synergistic effects of an increased molecular tumbling time (τ_R) and a faster proton exchange rate (τ_m).

GNTs also exhibit very large transverse relaxivities (r_2) at high magnetic fields ($\geq$ 3 T). The dependence of the transverse relaxation rates (especially R_2^*) of labeled cells on GNT concentration offers the possibility to quantify cell population *in vivo* using R_2^* mapping. The cell-labeling efficiency and high transverse relaxivities of GNTs has enabled the first non-iron oxide-based single-cell imaging using MRI.

The residual metal catalyst particles of SWNT materials also have transverse relaxation properties. All of the SWNT materials exhibit superior transverse relaxation properties. However, purified SWNTs and US-tubes with less residual metal content exhibit better transverse relaxivities (r_2), demonstrating the importance of the SWNT structure for enhanced MRI CA performance.

A strategy to improve the r_1 relaxivity of Gd-CAs by geometrically confining them within porous silicon particles (SiMPs) has been investigated. The enhancement in relaxivity is attributed to the slow diffusion of water molecules through the pores and the increase in the molecular tumbling time of the nanoconstruct. The universality of the strategy has been demonstrated for GNTs, gadofullerols and clinically-used Magnevist®.

In summary, primary nanoscale confinement of Gd^{3+} ions in US-tubes has resulted in a new class of CAs which could revitalize low-field contrast-enhanced MRI, while extending and complementing current high-field MRI technology, as well. The observed boost in relaxivity upon a secondary nanoscale confinement of Gd-CAs within SiMPs suggests that additional unforeseen nanoscale effects may have the potential to further boost performance of MRI CAs.

Acknowledgements

I want to express my heartfelt gratitude to my mentor and supervisor, Prof. Lon J. Wilson, for giving me the opportunity to work with him in his laboratory. I am eternally indebted to him for his guidance, support, and inspiration over the past five years. His invaluable mentoring has helped immensely in my personal and professional growth.

I am heartily thankful to the other members of my thesis committee: Dr. Robert Hauge, whose guidance and fruitful discussions greatly helped the successful completion of this thesis, and Prof. Enrique Barrera. I am happy to acknowledge Dr. Srinivasan, whose teaching and advice inspired me to pursue research. This thesis would not have been possible without the help and support of my collaborators. I am greatly indebted to them for their invaluable help with my experiments and my understanding of the subject. I am grateful to Prof. Paolo Decuzzi, Prof. Mauro Ferrari, Prof. Steven Wong, Prof. Murali Krishna Cherukuri, Dr. Shingo Matsumoto, Dr. Kelvin Wong, Dr. Tang Yi Mee, Prof. Edmund Lam, Prof. Ponnada Narayana, and Dr. Biana Godin-Vilentchouk for their guidance and countless hours of discussions.

I cannot overstate my deepest gratitude to the loving "Wilsonites," who never once made me feel away from home. I am especially grateful to Lesa Tran, Michael Matson, Sophia Phounsavath, Brandon Cisneros, Matthew Campbell, Richa Sethi, Matthew Cheney, Meghan Jebb, Scott Berger, Dr. Yuri Mackeyev, Adem Guven, Ari Berlin, and Eric Rutledge. I wish to thank Dr. Keith Hartman and Dr. Balaji Sitharaman for their support

and motivation. I am thankful to The Robert A. Welch Foundation, The Center for Biological and Environmental Nanotechnology at Rice University, and The National Institutes of Health for the financial support that helped carry out many of the studies presented in this thesis.

I owe my deepest gratitude to my sisters Sujatha and Sowmya, my brother-in-laws Ganesh and Murali, and my sweetest niece Teju for their love, care, and affection.

Lastly, but most importantly, I wish to thank my mom Visalam. She bore me, raised me, taught me, loved me, and still guides me. In her memory, I dedicate this thesis.

TABLE OF CONTENTS

Chapter III: Dextran-coated Individual Gadonanotubes (GadoDex) as CAs for MRI

Chapter IV: Part A: Gadonanotubes as T_2-weighted MRI CAs

Part B: Cellular Uptake and Single-Cell Imaging Using Gadonanotubes

Chapter V: Single-walled Carbon Nanotubes as T_2-weighted MRI CAs

List of Figures

List of Tables

CHAPTER 1

INTRODUCTION

Magnetic Resonance Imaging (MRI)

The 2003 Nobel Prize for Physiology or Medicine was awarded to Paul Lauterbur and Peter Mansfield in recognition of their contribution to what is now called magnetic resonance imaging (MRI). The first MR images of human were published in the 1977,[1] and ever since, MRI has evolved into one of the most powerful, non-invasive imaging modalities used in diagnostic medicine.[2] MRI is essentially an extension of nuclear magnetic resonance (NMR) spectroscopy, a widely-used characterization technique in the field of chemistry. The superior resolution, greater anatomical details, and excellent soft tissue contrast make MRI a preferred diagnostic imaging modality over other techniques such as computed tomography (CT) and ultrasound.[3, 4] In addition, the non-invasive nature of MRI helps in procedures involving imaging over longer periods of time.

Nuclear spin, an inherent property of water protons which are present in abundance in the human body, is manipulated by an external magnetic field to obtain magnetic resonance (MR) images. Each nuclear spin acts like a magnetic dipole, and in the absence of an external magnetic field, are oriented in random directions (**Figure 1a**). For a single spin system like ^{1}H, the application of an external field (B_0; along Z-axis) results in two different energy states: 1) a low-energy state corresponding to the alignment of nuclear spins parallel to the applied field and 2) a quantized high-energy state arising from anti-parallel alignment (**Figure 1b**). The population distribution of nuclear spins of these two energy states is determined by the Boltzmann distribution. Generally, a greater number of spins align parallel to the B_0 field (low energy state),

resulting in a net magnetization vector (NMV). The NMV precesses around the applied magnetic field (B_0) at a particular frequency known as the Larmor frequency (**Figure 1c**) given by the expression $\omega = \gamma B_0$ (γ is the gyromagnetic ratio specific for the NMR active isotope). When an external radiofrequency (RF) pulse (frequency = Larmor frequency) is applied in a direction perpendicular to the Z-axis, it excites the nuclear spin from the low-energy ground state (along the longitudinal or Z-axis) to the higher-energy excited state (along the transverse or XY-axis) (**Figure 1d**). Once the external pulse is removed after a short duration, the time taken for the excited state spin to return to its equilibrium position is termed the relaxation time. The relaxation process can occur via two mechanisms (**Figure 1e**): 1) relaxation along the axis of the applied magnetic field (longitudinal relaxation time; T_1) and 2) relaxation along the axis perpendicular to the applied magnetic field (transverse relaxation time; T_2).[4, 5]

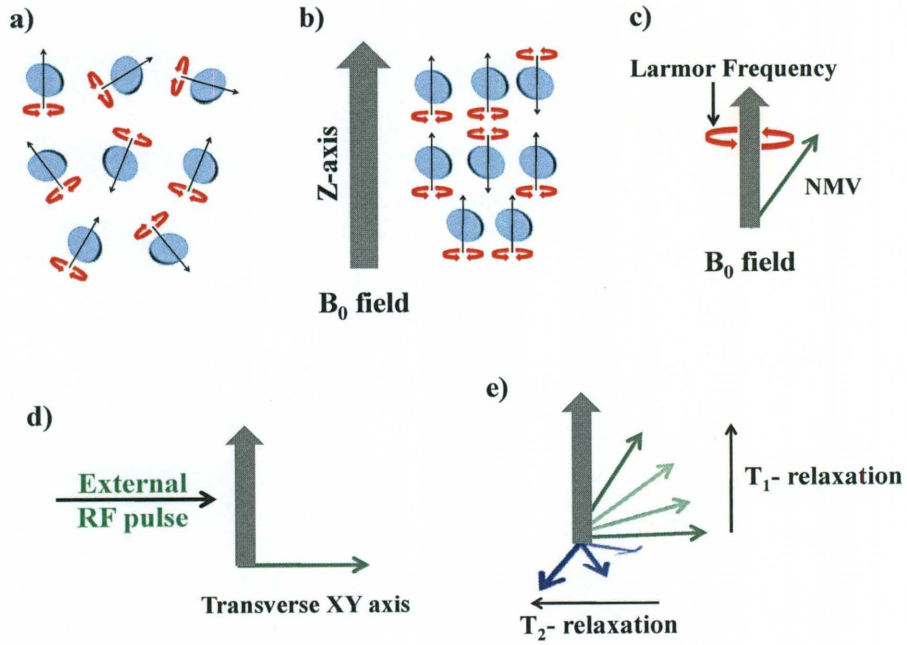

Figure 1. Schematic representation of proton relaxation mechanisms for MRI.

The intensity of the MR signal from a tissue is dependent on three important parameters, namely: 1) T_1-relaxation time of the tissue, 2) T_2-relaxation time of the tissue and, 3) the proton density in the tissue. Different tissues have different relaxation times (both T_1 and T_2) and proton densities. However, these differences are very subtle and require a variety of mathematical sequences to preferentially differentiate between the three parameters.

Role of Contrast Agents in MRI

Growing advancements in MRI led to the development of contrast agents (CAs) to improve the sensitivity and diagnostic confidence.[6, 7] In 2007, there were about 28 million MRI procedures performed in US alone, and nearly 45% of them used CAs for improving the diagnostic confidence.[8] CAs improve the sensitivity of MRI by decreasing the relaxation time of water protons in and around their vicinity. Most of the clinically-used CAs are paramagnetic in nature and, therefore, have a permanent magnetic moment. The magnetic moment of the paramagnetic ions exhibit a dipole-dipole interaction with magnetic moments of water protons in their vicinity and molecular motions cause random fluctuations to these dipolar magnetic interactions resulting in reduced T_1 and T_2 relaxation times. The reduction in the relaxation times of water protons is utilized to improve image contrast in MRI.[7, 9]

The high-spin paramagnetic Gd^{3+} ion is the most extensively used T_1 relaxation agent in MRI, since it has seven unpaired f-electrons (the maximum number of unpaired electrons observed for any atom or metal ion), a large magnetic moment (63 μ_B^2), and because of their symmetric ground sate (^8S), the Gd^{3+} ions exhibit slow electronic

relaxation properties. Slow electronic relaxation produces strong oscillations near the Larmor frequency and has a pronounced effect on the T_1 relaxation process.[6, 7]

Understanding the Relaxation Mechanism of Gd^{3+}-complexes

Aqueous Gd^{3+} ion is toxic and has to be sequestered for biological use. Traditional sequestering methods use a variety of linear and macrocyclic chelates (**Figure 2**), and the relaxation properties of these Gd^{3+}-chelate compounds have been extensively studied and characterized.[10] As mentioned above, the paramagnetic relaxation of water protons originates from dipole-dipole interaction between water protons and the fluctuating magnetic field caused by unpaired electrons in CAs. This fluctuating magnetic field vanishes rapidly with distance. Hence, for paramagnetic CAs to be effective, a mechanism by which the paramagnetic effect is transferred efficiently to the water protons surrounding the CAs is essential.[7]

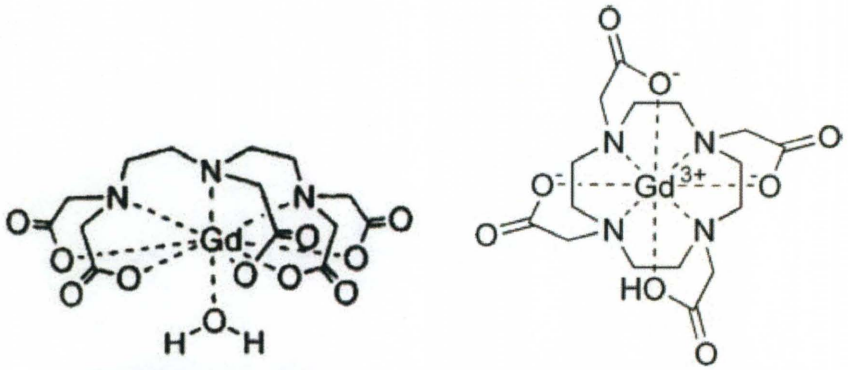

Figure 2. Depiction of Gd-chelate MRI CAs in clinical use.

There are two mechanisms by which the paramagnetic effect can be transferred to the bulk. The first mechanism (inner-sphere mechanism) involves the bonding of water molecules in the first coordination sphere of the metal ion. These inner-sphere water molecules then exchange with bulk protons propagating the paramagnetic effect. Thus, the inner-sphere mechanism depends on the number of water molecules (q) in the first coordination sphere of the metal ion, the residence time of the protons in the inner sphere (τ_m), and the molecular tumbling time (τ_R) of the paramagnetic CA with its inner-sphere water molecule. The second mechanism (outer-sphere mechanism) involves the random translation diffusion of water protons in the surrounding of the paramagnetic center. For most Gd^{3+}-chelate CAs, inner-sphere and outer-sphere mechanisms contribute equally (**Figure 3**).[11]

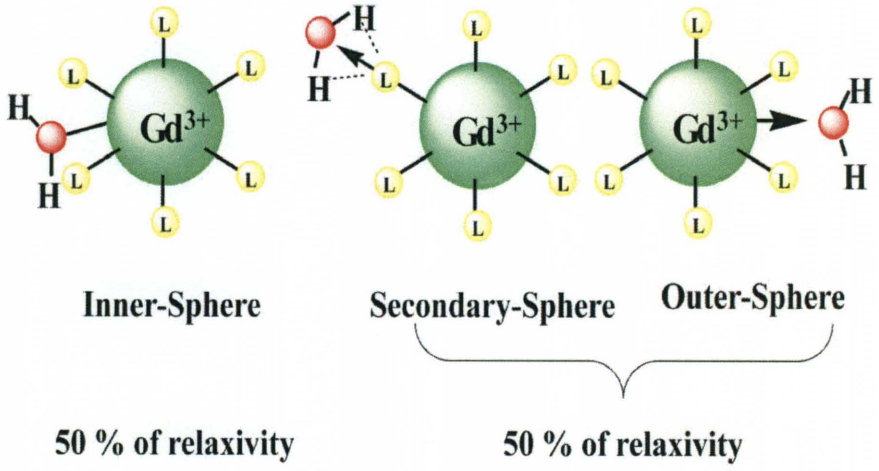

Figure 3. Schematic representation of contribution from inner- and outer-sphere relaxivity for Gd^{3+}-chelate CAs.

Considerable progress has been made in the synthesis and design of clinical Gd^{3+}-based CAs. In spite of all the progress, they still have several limitations. Chelation of the

Gd^{3+} ion with multidentate ligands decrease the number of coordination sites (q) available for water proton exchange (8 sites for free Gd^{3+} ion compared to 1-2 sites for Gd^{3+} chelate compounds), resulting in reduced relaxivity. Also, almost all of the clinically-used CAs are extracellular fluid space (ECF) agents with very low blood retention times (ca. 60 s), and they distribute extracellularly and excrete via the kidneys. For applications such as magnetic resonance angiography (MRA), agents with a longer blood plasma half-life are required. In addition, for cellular and molecular imaging using MRI, a very high relaxivity ($\geq$100 $mM^{-1}s^{-1}$) CA is required to compensate for the nM restriction in cell-surface receptor site concentration. [12] Current clinical CAs suffer from very low relaxivities ($r_1 \sim 4$ $mM^{-1}s^{-1}$) and therefore cannot be used for such applications. Hence, there is an important need to develop new MRI CAs with superior efficacies and more desirable physiochemical properties.

Carbon Nanostructure-based MRI Contrast Agents

The discovery of fullerenes, an allotrope of carbon, by Smalley, Curl, and Kroto marked the beginning of the field of "Carbon Nanotechnology".[13] The two main building blocks of Carbon Nanotechnology are: 1) fullerenes (C_{60}, C_{70}, C_{74}, C_{76} etc.), which are hollow and spherical or nearly-spherical molecules (**Figure 4a**) and 2) carbon nanotubes, which are hollow all-carbon cylindrical materials (**Figure 4b**). Single-walled carbon nanotubes (SWNTs) can be visualized as a single sheet of graphene rolled upon itself to assume the shape of a seamless cylinder.[14, 15] All the carbon atoms of these nanostructures are surface atoms, which produces a hollow, internal space within the nanostructures that can be potentially filled with medically-interesting atoms, ions, and even small molecules.[16, 17] When magnetically-active Gd^{3+} ions are encapsulated within

the interior of these highly-ordered nanostructures (Gadonanotubes; GNTs), a new class of MRI CA results.

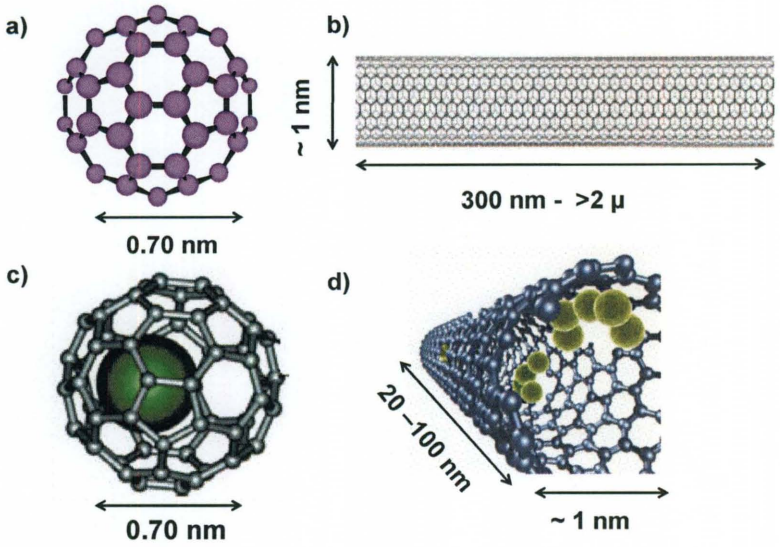

Figure 4. Building blocks of Carbon-based MRI CAs: a) C_{60} fullerene, b) single-walled carbon nanotube (SWNT), c) Gadofullerene (GF), and d) Gadonanotube (GNT).

Gadonanotubes as MRI Contrast Agents

Nanoscale loading and confinement of Gd^{3+} ions inside ultra-short single-walled carbon nanotubes (US-tubes) resulted in a high-performance MRI CA, Gadonanotubes (GNTs; **Figure 4d**).[18] The Gd^{3+} ions are present in the form of clusters located at the defect sites on the sidewalls of the US-tubes which are produced during the SWNT cutting process. The GNTs resemble linear superparamagnetic molecular magnets with ^1H relaxivities 40-90 times greater than any current Gd^{3+}-based CA in clinical use. Because of the hydrophobic nature of the US-tubes, GNTs do not disperse well in water. However, a variety of biocompatible surfactants have been used to impart

biocompatibility to GNTs. The relaxivities (per Gd^{3+} ion) of the GNTs dispersed in different surfactants, along with the aqueous $[Gd(H_2O)_8]^{3+}$ ion, are presented in **Table I** at a clinically-relevant field strength of 1.41 T. The r_1 relaxivity of the GNT is about 20 times greater than that of the $[Gd(H_2O)_8]^{3+}$ ion at 1.5 T. When compared to clinically-used Gd^{3+}-based CAs, GNTs are about 40 times more efficacious at 1.5 T.

Table I. Longitudinal proton relaxivities of GNTs. Measurements were performed at 60 MHz and 37 °C. ǂ: dispersed in sodium dodecyl benzene sulfonate (SDBS), +: dispersed in Pluronic.

	$[Gd^{3+}]$ (mM)	Relaxation rate (s^{-1})	$r_1(mM^{-1}s^{-1})$ (per Gd^{3+} ion)
Gadonanotubes ǂ	0.044	7.85	173
Gadonanotubes +	0.049	8.29	164
$[Gd(H_2O)_8]^{3+}$	1.99	16.95	8.4

Advantages of Gadonanotube Contrast Agent

GNTs as MRI CAs offer several unique advantages over current clinically-used Gd^{3+}-based CAs, such as:

1) The Gd^{3+} ions are trapped within a biologically-stable carbon cage (carbon nanotubes), preventing the release of toxic, free Gd^{3+} ions. In contrast, some clinical CAs are susceptible to the release of Gd^{3+} ion, especially in patients with kidney disease, leading to nephrogenic systemic fibrosis (NSF).[19]
2) The external all-carbon surface of GNTs can be chemically functionalized to control toxicity, enhance biocompatibility, and provide targeting ability using antibodies and/or peptides.[20, 21]

3) The nanoscale confinement of Gd^{3+} ions inside the carbon nanotubes provides them with an unusual metal-ion environment, resulting in remarkably high relaxivities (r_1 >100 $mM^{-1}s^{-1}$ per Gd^{3+} ion). In fact, the GNTs are the highest performing T_1-weighted MRI CA known, making them especially desirable candidates for future applications in molecular imaging.
4) The inherent lipophilicity of GNTs provides them the ability to efficiently translocate across cell membranes, without evidence of cytotoxicity. Once target cells are internally labeled with GNTs in sufficient concentration, high-resolution cellular imaging using MRI may well be achievable.

This work details the development of GNTs as high-performance CAs for advanced imaging applications such as cellular and molecular imaging using MRI.

CHAPTER 2

Gadonanotubes as Low-field MRI Contrast Agents

Introduction to Low-field Magnetic Resonance Imaging

Magnetic resonance imaging (MRI) scanners are generally classified into three types on the basis of the magnetic field strength: 1) low-field MRI scanners (< 0.5 T), 2) mid-field MRI scanners (0.5-1.0 T), and 3) high-field MRI scanners (1.0 T and above). Most of the high-field instruments use expensive cryogenically-cooled superconducting magnets to generate the magnetic fields. The high cost associated with high-field instruments limits the use of MRI as an imaging modality for all diagnostic purposes.[22, 23] The main motivation behind the development of low-field scanners is their cost-effectiveness. Low-field systems also offer other advantages, such as an "open" design suitable for interventional MRI and less contraindications (associated with imaging patients with metallic implants). However, the main disadvantage with low-field systems is the low signal-to-noise ratio (SNR) resulting in lower resolution of images. In addition, most tissues exhibit lower relaxation times (T_1 and T_2) at low magnetic field strengths.[24, 25] Even though there is no conclusive evidence of low-field MRI (and its low resolution) adversely affecting diagnostic outcome, high-field systems are more popular for diagnostic imaging.[23] To circumvent the low resolution of low-field MRI systems, longer scan times have been proposed. However, longer scan times can result in greater image degradation due to patient movement. In addition, CAs have been used improve the SNR in low-field MR images (**Figure 5**). However, many of the clinically-used T_1-weighted MRI CAs (mainly Gd-based complexes) have very low efficiency and exhibit little or no field-dependency in their contrast enhancement properties, as exemplified by

the Magnevist® data on **Figure 6**. It has been observed that, to obtain a comparable resolution at lower magnetic fields, at least twice the amount of CA (compared to high-field scans) must be administered to the patients.[26, 27] Such high doses are not advisable, since clinically-used Gd-based CAs are alleged to cause nephrogenic systemic fibrosis (NSF) in some patients with renal dysfunction.[28] We have reported that GNTs are high-performance MRI CAs with relaxivity (contrast enhancement efficacy) ~40 times greater than that of current clinical Gd-based agents at 1.5 T (**Figure 6**).[18] Unlike other Gd-based agents, GNTs exhibit much higher relaxivities at lower magnetic field strengths (**Figure 6**). The extremely high r_1 relaxivity (as high as 600 mM^{-1}-s^{-1}) should overcome the low resolution associated with low-field MRI. In addition, cellular and molecular imaging using MRI requires very high-relaxivity agents ($r > 100$ $mM^{-1}s^{-1}$) accompanying with cell-labeling efficiency.[12] The lack of efficient intracellular labeling for current Gd-based CAs and their very low relaxivity (~ 4 $mM^{-1}s^{-1}$) have alternatively resulted in the development of iron oxide (SPIO)-based CAs for cellular and molecular imaging.[29, 30] However, SPIO-based CAs (T_2-weighted CAs) belong to the negative CA category (darkening of the image) and create signal voids in its proximity. Such signal voids are hard to differentiate from hypointense signals arising from other sources. This drawback has greatly limited the progress of MR molecular imaging. The lipophilic nature of GNTs provides them with the ability to translocate through cell membranes without the aid of transfection agents or advanced labeling techniques. The efficient intracellular localization for GNTs, along with their very-high relaxivity at all field strengths, has produced the opportunity for a new paradigm in MR molecular imaging. In this chapter,

the ability of GNTs to function as powerful T_1-weigthed, low-field MRI CAs and their potential for cellular and molecular imaging at low fields is considered in detail.

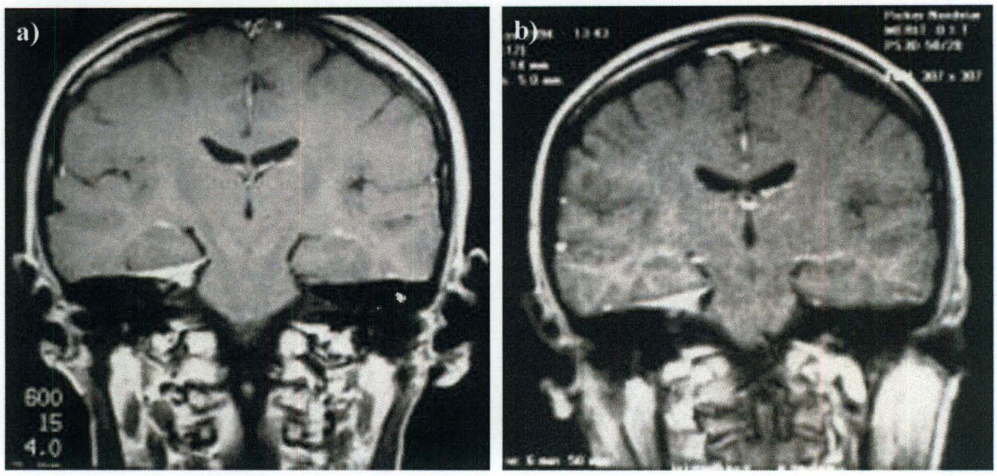

Figure 5. Contrast-enhanced T_1-weighted images of skull base meningioma at a) 1.5 T (slice thickness 4 mm) and b) 0.1 T (slice thickness 4 mm) using the same image acquisition settings. Both the images are equally diagnostic but *image a* shows higher resolution. Reproduced with permission from Ref 27.

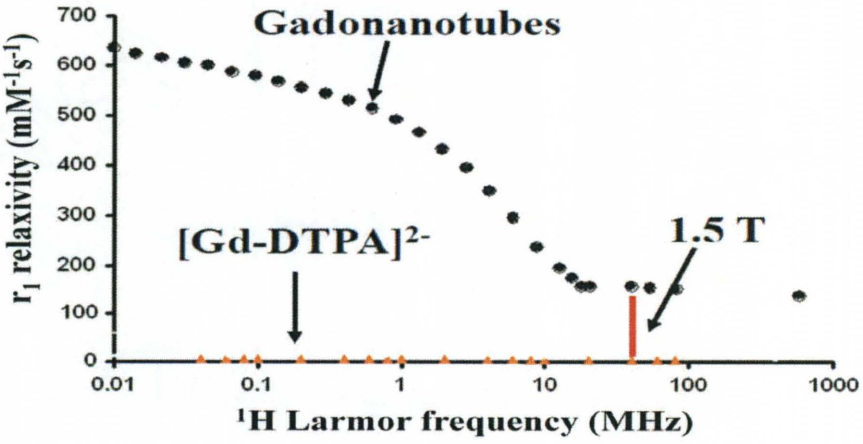

Figure 6. Nuclear Magnetic Relaxation Dispersion (NMRD) profile for bundled GNTs (dispersed in SDBS). For comparison, NMRD profile of a clinically-used CA, (Magnevist®;[Gd-DTPA]2-), is also presented. The measurements were performed at 37 °C.

MATERIALS AND METHODS

Synthesis of GNTs

GNTs were synthesized using our published protocol.[18] Briefly, full-length single-walled carbon nanotubes produced by electric arc discharge process were cut into ultra-short tubes (US-tubes) of 20-80 nm in length by fluorination followed by pyrolysis at 1000 °C in an inert Ar atmosphere.[31] As obtained US-tubes were sonicated with concentrated HCl to remove metal catalyst impurities. Due to their hydrophobic nature, US-tubes exist in the form of various-sized bundles. Part of the US-tubes was reduced using Na^0/THF to generate predominantly individual US-tubes.[16] Both the bundled US-tubes and individual US-tubes were loaded with Gd^{3+} ions using a simple aqueous loading method. Briefly, 100 mg of US-tubes (bundled or individual) were added to 100 mL of aqueous $GdCl_3$ solution (1 mg/mL) and bath sonicated for 60 minutes. The solution was allowed to settle overnight. The gadolinium-loaded US-tubes (Gadonanotubes; GNTs) flocculated at the bottom. The supernatant was discarded and flocculated GNTs were washed repeatedly with DI water to remove any external Gd^{3+} ions adhering to the US-tube sidewalls. **Figure 7** shows the schematic representation of an individual GNT.

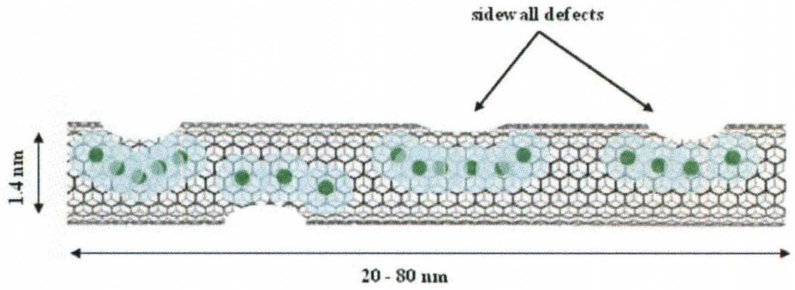

Figure 7. Schematic representation of an individual GNT.

For MRI phantom measurements, solutions of bundled GNTs and individual GNTs were prepared using 1.0 % solution of a biocompatible Pluronic® surfactant (polyethylene oxide-polypropylene oxide block copolymer). In addition, a solution of individual GNTs coated with carboxylated dextran (GadoDex) was also prepared. The synthesis and characterization of GadoDex is discussed in detail in Chapter 3. The Gd^{3+} content of each phantom was determined using inductively-coupled plasma optical emission spectrometry (ICP-OES, Perkin-Elmer Optima 3200V). GNT phantoms had final Gd^{3+}-ion concentrations of (a) 104 μM for bundled GNTs (b) 83 μM for individual GNTs, and (c) 39 μM for GadoDex, respectively. For comparison, a solution of clinically-used Gd-based CA, Gd-DTPA (Magnevist®), at 20 mM Gd^{3+} was prepared in sterile physiological saline. All the samples were sealed in cylindrical containers of 1 cm diameter.

In Vitro Phantom Imaging

MRI experiments were performed using a 0.2 T open MRI system (Signa Profile, General Electric, Milwaukee, WI). The system was interfaced with a Tecmag Apollo console (Tecmag, Houston, TX). The GNT and Gd-DTPA solutions were aligned in a single row at the iso-center of the magnetic bore, with the cylinder axis perpendicular to the main magnetic field. A standard quality assurance ball-shaped MRI phantom from the manufacturer was used and placed on top of the solution phantoms to ensure proper shimming. To obtain the relaxation curve for T_1 value calculations, a 2D gradient echo sequence (GRE) (matrix = 256 x 256, FOV = 30cm, alpha = 90°, NEX = 1) with TE = 6 ms and various TRs (18 ms, 25 ms, 50 ms, 100 ms, 150 ms and 200 ms) were used consecutively. The maximum TR of 200 ms was chosen based on prior knowledge that it

allowed full recovery of longitudinal magnetization. A single slice of 10 mm thickness cut across all samples perpendicular to their cylinder axis was obtained for each TR. The mean signal intensity of each phantom at each TR was determined by drawing a circular region of interest (ROI) of equivalent size on each phantom. The background image noise was obtained by drawing 64 x 64 pixels ROI at the image background, and was fitted and suppressed from the mean signal intensity of each phantom with a Rician distribution noise model. The mean ROI signal intensity of each phantom was used in the determination of the T_1 value, if the measurement was not at noise level ($p < 0.05$). To obtain the relaxation curve for T_2 value estimation, a spin echo sequence (SE) was employed with a fixed TR = 1000 ms and various TEs (6.5 ms, 7 ms, 8 ms, 10 ms, 20 ms, 25 ms, 50 ms, and 100 ms). The same slice orientation and mean signal intensity measuring method was used to obtain the relaxation curve for T_2 value estimations.

Cell Labeling and Imaging with GNTs

A NIH 3T3 mouse fibroblast cell line was cultured at 37 °C and 5% CO_2 in 100 x 20 mm tissue culture dishes using standard cell culture media, containing Dulbecco's Modified Eagle Medium (DMEM, Invitrogen) with 10% fetal calf serum (FCS, Invitrogen) and 1% Penicillin-Streptomycin (S/P, Fisher Scientific). For cell labeling experiments, 10^7 cells/well were plated for 24 hours to allow cell adhesion. The cells were then incubated with GNT solution diluted with the standard culture media (final [Gd] = 0.01 μM, 0.025 μM, 0.5 μM, 1.0 μM, and 5.0 μM) for 24 hours. The labeled cells were then washed twice with phosphate-buffered saline (PBS, Invitrogen) to remove any excess GNTs that might be adsorbed on the cell membrane. The labeled cells (~ 2.5 × 10^7) were resuspended in 1.2 mL of PBS and centrifuged at 1000 rpm for five minutes to

make a pellet. The cell pellets were imaged in a 15 mT scanner using TR/TE = 120/25 ms and NEX = 64. Unlabeled cell pellets were used as a control.

RESULTS AND DISCUSSION

Magnetic Characterization in a 0.2 T Clinical MRI Scanner

Figure 8 represents the T_1-weighted MRI phantoms of GNTs along with clinical MRI CA, Magnevist®. All the three GNT samples exhibit a very strong T_1 effect, as observed by the increase in image intensities with increasing TR (the time interval between successive RF pulses applied on the same sample slice). The effect is more pronounced for individual GNTs and GadoDex, where the image intensities are much brighter. In contrast, Magnevist® showed no observable contrast enhancement. The lack of enhancement is more significant considering that the $[Gd^{3+}]$ in Magnevist® (20 mM) is ~ 200 - 500 times greater than that of GNTs.

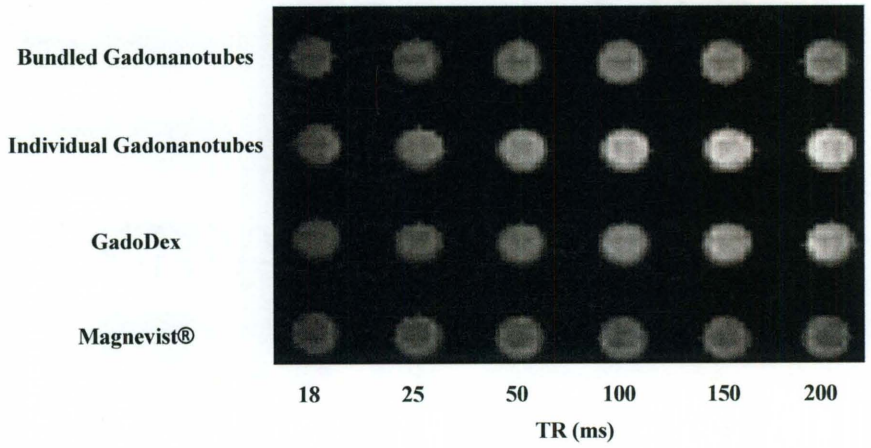

Figure 8. T_1-weighted phantom images of GNTs compared with the clinically-used MRI CA, Magnevist®, in a 0.2 T scanner at 25 °C.

However, the image intensities in **Figure 8** are not the true representation of the relaxation efficacy (relaxivity) of the sample. The image intensities are dependent on the concentration, and all the samples have different Gd^{3+}-ion concentrations. In order to compare their efficacy, their T_1-shortening (contrast enhancement) properties have to be normalized for the Gd^{3+}-ion concentration. The efficacy, which is normalized for Gd^{3+}-ion concentration, is called relaxivity ($r_{1,2}$; $mM^{-1}s^{-1}$) and is calculated using the expression $r_{1,2} = R_{1,2} - R_0/[CA]$, where R_1 is the relaxation rate ($1/T_1$; s^{-1}) of water protons in the presence of CA, and, R_0 is the relaxation rate in the absence of CA, and [CA] is the concentration of CA in mM.[32] The T_1 values of all the four samples were calculated from the mean signal intensities (S_i) from **Figure 8** using the equation, $S_i = S_0 . (1 - e^{-TR/T1})$. S_0 is the signal intensity at equilibrium state; TR is the repetition time of RF pulses. All of the fits in **Figure 9** exhibited R^2 values ≥ 0.99, suggesting a good fit to the experimental data.

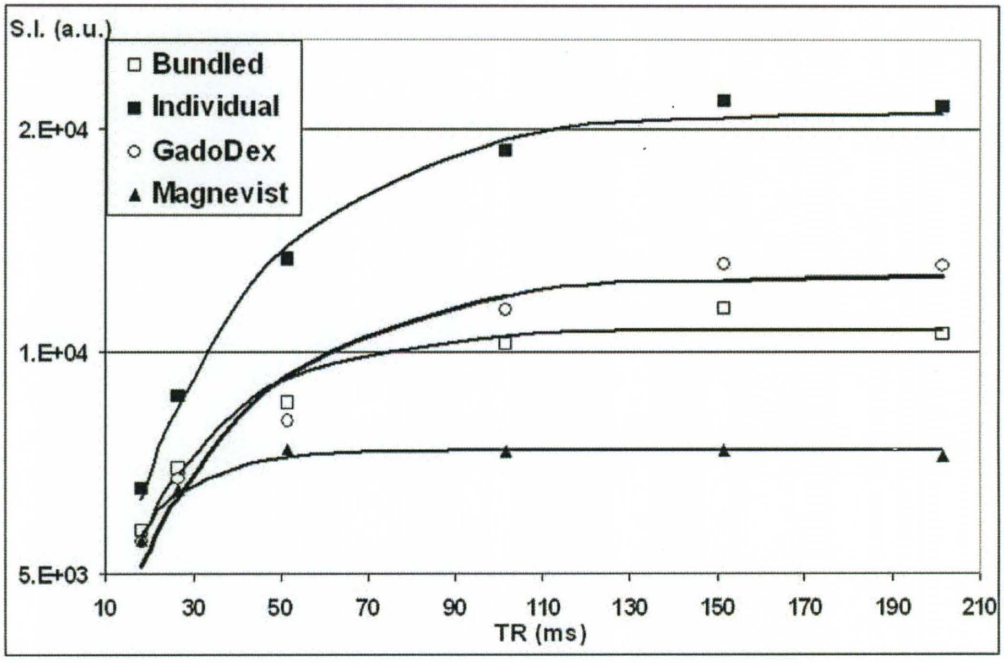

Figure 9. Fitting of signal intensities for T_1 calculation of GNTs and Magnevist® at 0.2 T.

Table II. Comparative relaxivities of Gd-based MRI CAs at 0.2 T.

Sample	[Gd] mM	T_1 (ms)	T_2 (ms)	r_1 ($mM^{-1}s^{-1}$) per Gd^{3+} ion	r_2 ($mM^{-1}s^{-1}$) per Gd^{3+} ion	r_2/r_1
Bundled GNT	0.104	22.64	28.57	418	314	0.75
Individual GNT	0.083	31.60	38.46	373	285	0.76
GadoDex	0.039	31.14	70.42	806	303	0.37
Magnevist®	20	12.94	8.5	3.8	5.8	1.52

As can be seen from **Figure 9** and **Table II**, GNTs have a dominant T_1-shortening effect at low-fields. Their relaxivity values suggest that GNTs are better than the current clinically-used agent by at least two orders of magnitude. A T_1-weighted CA is required to have a more pronounced effect ($r_2/r_1 < 2$) on the longitudinal relaxation (T_1-shortening) of water protons than on their transverse relaxation (T_2-shortening).[32] All the Gd-based CAs compared in the above studies are good T_1-weighted CAs; however, GNTs are much better than Magnevist®. The r_2/r_1 ratio for GNTs makes them attractive candidates for cellular and molecular imaging using T_1-weighted MRI at low-fields. In addition, the exceptionally large relaxivities of GNTs suggest that even a smaller concentration of GNTs can produce higher contrast when used at low fields. This effect is especially pronounced for GadoDex, since its relaxivity (806 $mM^{-1}s^{-1}$ per Gd^{3+} ion) is the greatest, by far, ever reported for any Gd-based CA under any conditions!

Cellular Imaging at 15 mT MRI Scanner

For the cell labeling experiments, individual GNTs are preferred over bundled GNTs because of sample homogeneity. However, as with many other low-field scanners, the 0.2 T scanner we used was discarded for the want of space. Hence, most of the

previous low-field data had to be recollected with the 15 mT scanner available at National Institutes of Health (NIH), Bethesda, Maryland. Unlike the 0.2 T scanner (a commercial scanner), the new 15 mT scanner was a custom built scanner designed for hyperpolarized MRI studies. As a result, the pulse sequences and other imaging parameters were limited. Before cell labeling and imaging using GNTs, the efficacy of individual GNTs dispersed in Pluronic surfactant was first tested at 15 mT. The phantom image of GNTs and Magnevist® at 15 mT is presented in **Figure 10**.

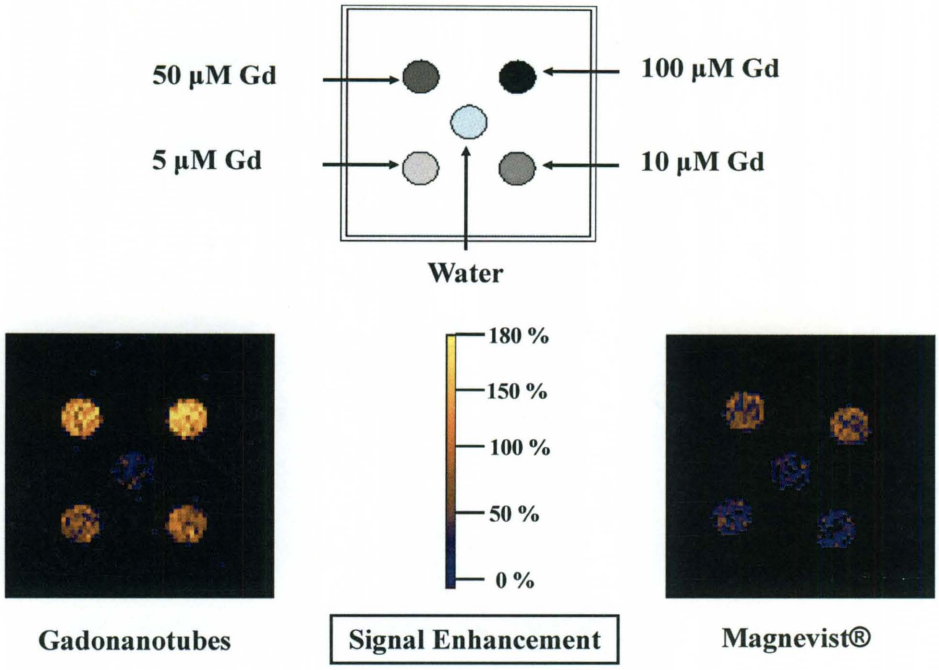

Figure 10. T_1-weighted phantom images (15 mT) of individual GNTs and Magnevist® at different Gd^{3+}-ion concentration. The measurements were performed at room temperature.

GNTs exhibited better contrast enhancement than Magnevist® at 15 mT, reiterating their superior T_1-shortening properties at low-field strengths. However, the

relaxivity of individual GNTs at 15 mT were significantly lower (~ 50 %) than the relaxivity values at 0.2 T (**Figure 11**).

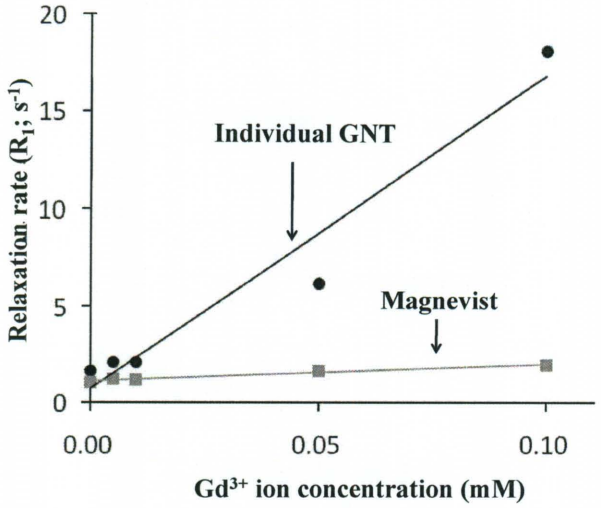

Sample	r_1 ($mM^{-1}s^{-1}$) per Gd^{3+}-ion (0.2 T)	r_1($mM^{-1}s^{-1}$) per Gd^{3+}-ion (0.015 T)
Individual GNT	373	162
Magnevist ®	3.8	8.7

Figure 11. Relaxivity (r_1) calculation of individual GNTs and Magnevist® at 15 mT and comparison of relaxivity values for 0.2 T and 15 mT.

The observed difference in relaxivities between the 0.2 T and 15 mT magnetic fields is most likely due to the difference in the image acquisition parameters for the two instruments. The 0.2 T scanner used was a commercial unit. Hence, it has many optimized pulse sequences compared to the 15 mT scanner used for the most recent studies. In spite of reduced relaxivities at 15 mT, GNTs are still ~20 times more efficacious than Magnevist®. This has significant importance as the current trend in low-field MR imaging is to use twice the concentration of Gd-based CAs to obtain similar resolution as that of high-field instruments.[26, 27]

In order to test the efficacy of GNTs to act as cell labeling and imaging agents at low-fields, mouse fibroblast cells (NIH 3T3) were labeled with GNTs. The inherent lipophilicity of GNTs enabled efficient cell labeling without the aid of transfection agents

or advanced cell labeling techniques. A control phantom with unlabeled fibroblast cells was also imaged at 15 mT. Different incubation concentrations of individual GNTs resulting in final Gd^{3+}-ion concentration of 0.01 μM, 0.025 μM, 0.1 μM, 0.5 μM, and 5 μM were used. At higher incubation Gd^{3+}-ion concentrations (0.1 μM, 0.5 μM, 5 μM), no contrast enhancement in GNT-labeled cells was observed (**Figure 12**). In fact, the GNT-labeled cells appeared darker than unlabeled control cells, suggesting a dominant T_2^* (spin-spin relaxation) effect. Interestingly, at lower incubation Gd^{3+}-ion concentrations (0.025 μM, 0.010 μM), the GNT-labeled cells appeared brighter than unlabeled cells.

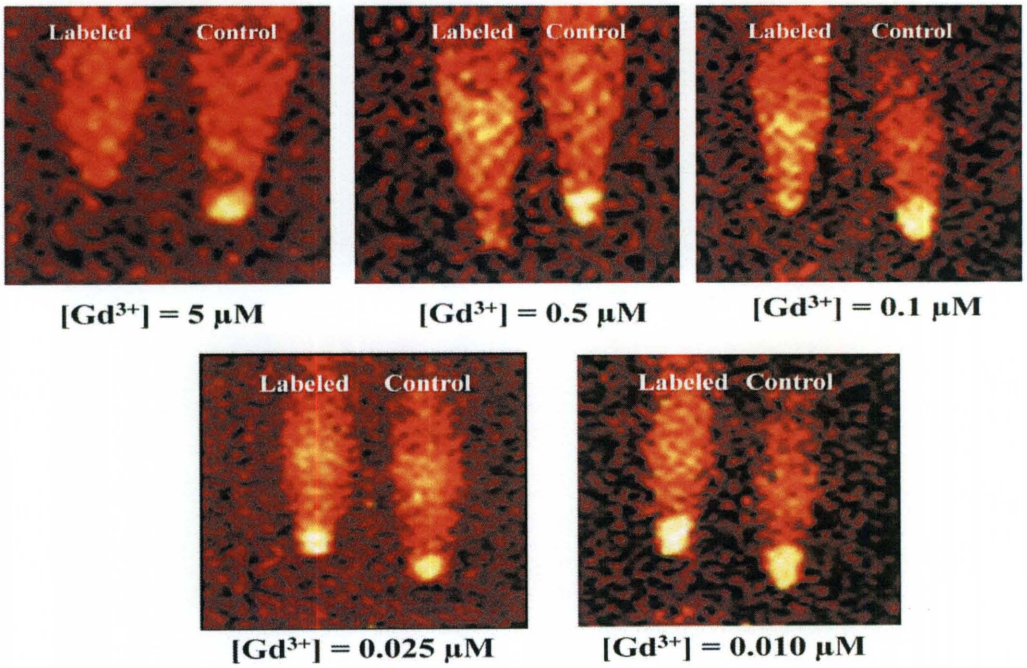

Figure 12. T_1-weighted MRI phantom images of GNT-labeled cells at 15 mT for different incubation Gd^{3+}-ion concentrations.

The T_2^* effect observed at higher incubation concentration is likely due to dense packing of GNTs inside the cells. In a separate experiment (result not shown), we

demonstrated that the amount of GNTs localized within a cell is directly proportional to the incubation concentration. Hence, at higher incubation concentration, more GNTs will be present within the cell resulting in a dense packing. Such close packing of CAs have previously been shown to result in susceptibility effects leading to greater enhancement in T_2^* effect in superparamagnetic iron-oxide labeled cells.[33-35] The superparamagnetic nature of GNTs (see **Chapter 4**) suggests that such a mechanism is possible for GNT-labeled cells as well. At lower incubation Gd^{3+}-ion concentrations (0.01 μM, 0.025 μM), the GNTs localized within the cell should experience less aggregation. In such cases, the susceptibility-induced T_2* effect should be less pronounced leading to enhanced contrast of labeled cells compared to control cells (**Figures 12 and 13**).

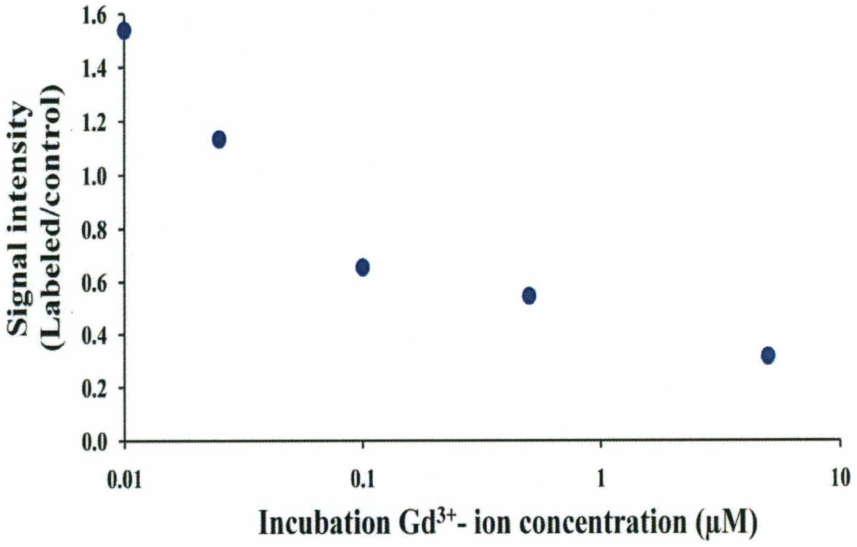

Figure 13. T_1-weighted contrast enhancement for GNT-labeled cells as a function of incubation Gd^{3+} concentration at 15 mT and 37 °C.

The enhancement in contrast at lower Gd^{3+}-ion concentration when intracellularly localized is an interesting and very useful property of GNTs. Current cellular and

molecular imaging using MRI mainly revolves around superparamagnetic iron oxide based T_2-weighted CAs. To be able to visualize the cells using MRI and track them *in vivo,* extensive labeling (~20 pg Fe/cell) is required.[30] In such a scenario, after a few cell division cycles, the iron concentration becomes too diluted to enable further tracking of labeled cells. Our results suggest that GNT-labeled cells can initially be imaged using T_2-weighted MRI and then, even after multiple cell divisions, can still be tracked using their very efficient T_1-shortening properties at lower concentrations. The ability to image the same CA based on two different relaxation mechanisms by altering their intracellular concentration is hitherto unknown for any MRI CAs and is a potential advantage for GNTs that needs further investigation.

CONCLUSION

Low-field MR imaging has long suffered from low SNR that limits its use in clinical diagnosis. GNTs with their extremely large longitudinal relaxivities (as high as 800 $mM^{-1}s^{-1}$) offer a new paradigm in contrast-enhanced low-field MRI. The lipophilic nature of GNTs provides them with the ability to translocate through the cell membrane without the aid of transfection agents or other advanced cell-labeling techniques. The cell labeling efficiency and the superior low-field relaxivities of GNTs projects a new class a T_1-weighted CAs for cellular and molecular imaging. If translated to real-time imaging applications, the observed contrast enhancement with lower intracellular Gd^{3+} concentration may well lead to a new class of MRI CAs with the potential for long-term *in vivo* tracking in stem cell therapy and drug delivery applications.

CHAPTER 3

Dextran-coated Individual Gadonanotubes (GadoDex) as CAs for MRI

Need for Biocompatible, Protein-resistant Coating

GNTs exhibit longitudinal relaxivities (~ 170 $mM^{-1}s^{-1}$) 40-50 times greater than clinically-used Gd-chelates (~ 4 $mM^{-1}s^{-1}$).[18] GNTs also show unprecedented pH sensitivity which could help in the early detection of disease.[36] The hydrophobic nature of the single-walled carbon nanotube (SWNT) necessitates the use of surfactants/polymers to disperse GNTs for biological applications. A variety of surfactants and synthetic polymers have been proposed for the dispersion of SWNTs.[37] A biocompatible Pluronic® (PEO-PPO block copolymer) has been successfully used for GNT dispersion. However, it has been shown that the Pluronic coating is replaced very quickly by proteins in the bloodstream.[38] Such fast adsorption of proteins on the SWNT surface is not ideal for the development of GNTs as vascular agents or targeted MR imaging. For a successful vascular agent and targeted delivery, it is important that the agent stays in the bloodstream for longer time periods (longer blood circulation time). For achieving long circulation times, many natural and synthetic polymers have been proposed and studied. Dextran, a polysaccharide made of sucrose units, has been shown to have a protein-resisting surface.[39, 40] It is also used to solubilize iron oxide for use in MRI.[41] In this Chapter, the development of dextran-coated GNTs (GadoDex) and their efficiency as a longitudinal MRI CA is reported.

MATERIALS AND METHODS

Synthesis of GadoDex

GNTs (bundled and individual) were synthesized using the protocol detailed in **Chapter 2**. Dextran with an average molecular weight of 9,000-11,000 Da was purchased from Sigma–Aldrich (St Louis, Mo). As obtained dextran was carboxylated using a procedure reported by others.[42] Briefly, 2 g of dextran was dissolved in 10 mL of DI water. To this, 0.2 mL of 40 % NaOH was added and the solution was refluxed for 45 minutes. The solution was then allowed to cool down to room temperature and the carboxylated dextran was precipitated using methanol (**Figure 14**).

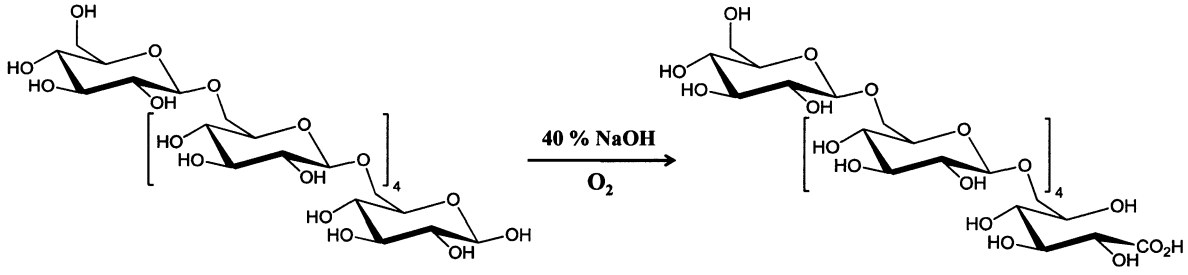

Figure 14 Schematic representation of the synthesis of carboxylated dextran.

Individual GNTs (25 mg) were then refluxed with 25 mL of carboxylated dextran solution in DI water for 45 minutes. The resulting suspension (GadoDex) was then probe-sonicated for 2 minutes and allowed to settle overnight. The solution was centrifuged at 3,200 rpm for ten minutes to remove large aggregates and unwrapped GNTs. The supernatant was then dialyzed against running water (50,000 MW cutoff membrane) for three days to remove any unreacted carboxylated dextran.

Characterization

The solubility measurements were carried out in a UV-Vis spectrometer. For solubility measurements, known amounts of lyophilized GadoDex were dissolved in a known volume of water. The absorbance spectrum was collected for different concentrations of GadoDex in solution. The maximum solubility was taken as the concentration at which the absorbance ceased to increase linearly with increasing GadoDex concentration. The atomic force microscopy (AFM) imaging was then performed using a Nanoscope II instrument. Typically, 20 μL of the GadoDex solution (5mg/mL) was spin-coated on a mica disc and used for the imaging studies. Transmission electron microscopy (TEM) images were taken with a JEOL 2010 transmission electron microscope using a lacey carbon grid.

The Gd^{3+}-ion concentration was measured using inductively-coupled plasma-optical emission spectrometry (ICP-OES). The samples for ICP-OES measurements were prepared by digesting a known volume of GadoDex with 90 % HNO_3 (heated carefully to dryness) followed by 30 % H_2O_2. The solid residue thus obtained was dissolved in 2% HNO_3 and used for ICP measurements.

The relaxation measurements were performed using a bench-top relaxometer (Bruker Minispec mq 60) at 60 MHz and at 37 °C. An inversion recovery pulse sequence was used for longitudinal relaxation time (T_1) measurements.

Nuclear Magnetic Relaxation Dispersion (NMRD) Profile

NMRD measurements were performed using a Stelar Spinmaster FFC fast field cycling relaxometer covering a continuum of magnetic fields from 2.35×10^{-4} to 0.47 T

(corresponding to proton larmor frequency of 0.01 - 20 MHz) equipped with a VTC 90 temperature control unit. For relaxivities at higher fields, Bruker Minispec mq30 (30 MHz), mq40 (40 MHz) and mq60 (60 MHz) and Bruker 1.18 T (50 MHz), 2.35 T (100 MHz) and 4.70 T (200 MHz) cryomagnets connected to a Bruker Avance-200 console were used.

Phantom Measurements in Clinical Scanner

Clinical MRI phantom measurements were performed with a 3 T Intera MRI system (Philips Medical Systems, Best, Netherlands) with a Quasar gradient system (Philips Medical Systems). For T_1 measurements, multiple inversion recovery sequences were used with identical TE and varying inversion time (TE/TR/TI = 10/10000/200, 400, 800, 1000, 1500, 2000, 2500, 3000, 4000, 5000 ms). Each image was acquired in the coronal plane with 128 x 128 matrix over a 150 mm x 150 mm FOV, with slice thickness of 3 mm. Slice locations for T_1 were reproducibly placed at the same locations in the phantom using a high-resolution 3D magnetization-prepared rapid gradient echo (MPRAGE) sequence for localization.

RESULTS AND DISCUSSION

Characterization of GadoDex

Full-length SWNTs have been shown to be very well-dispersed in a 1% dextran solution.[43] In our studies, bundled GNTs also dispersed well in the aqueous dextran solution. Biological applications involving SWNTs require homogeneous distribution. Hence, individual GNTs (predominantly single tube or small bundle of 2-3 tubes) were prepared in the same way as that of bundled GNTs. Interestingly, individual GNTs lacked

solution stability when sonicated with an aqueous solution of dextran (2% (w/v) in DI H_2O) and precipitated quickly after sonication. To achieve a stable dispersion of individual GNTs coated with dextran, it was decided to try carboxylated dextran. Carboxylated dextran has been widely used to solubilize iron oxide-based CAs. Dextran-coated iron oxide particles are commercially used for imaging liver and spleen and are currently in clinical trials for other imaging applications.[41, 44] The carboxyl groups on the dextran molecule interact strongly with the iron atoms on the surface of the iron oxide nanoparticles to form a stable dispersion for biological applications.[42] Our hypothesis is that such interactions are also possible with GNTs since Gd^{3+} ions (located at the defect sites in GNTs) are known to be strongly chelated by the carboxyl groups. Upon refluxing GNTs with a carboxylated-dextran solution, followed by sonication, a stable dispersion of individual GNTs (GadoDex) resulted. We believe that this stable dispersion is likely due to the interaction between the carboxyl groups of dextran and the Gd^{3+} ions of GNTs. Carboxylates have long been known as excellent chelators for metal ions and many of the current Gd-based clinical MRI CAs are polyaminocarboxylate complexes of Gd^{3+}.[10] The likelihood of carboxylate-Gd^{3+} interaction in GadoDex is further corroborated by the observation that individual US-tubes (no Gd^{3+} ions) lacked stability in solution when refluxed with a carboxylated-dextran solution. The potential downside of carboxylate-Gd^{3+} interaction is that strong chelation of Gd^{3+} ions might result in possible leakage of Gd^{3+} ions from US-tubes. It is believed that the Gd^{3+}-ion clusters are central to the superior relaxivity exhibited by GNTs over other clinically-used paramagnetic Gd-based MRI CAs.[18] To confirm the stability of the Gd^{3+}-ion clusters in GadoDex, we analyzed the washings from the dialysis of GadoDex by ICP-OES. If Gd^{3+} ions leaked from GNTs

due to strong carboxylate-Gd^{3+} interactions, they should be removed by the dialysis process due to their small size. No such leakage of Gd^{3+} ions was detected by ICP-OES measurements (sensitivity 1 ppb). The dialyzed GadoDex was also characterized for its magnetic properties. The SQUID magnetic measurements post-dialysis showed that GadoDex retained the superparamagnetic nature of the original GNTs (**Figure 15**).

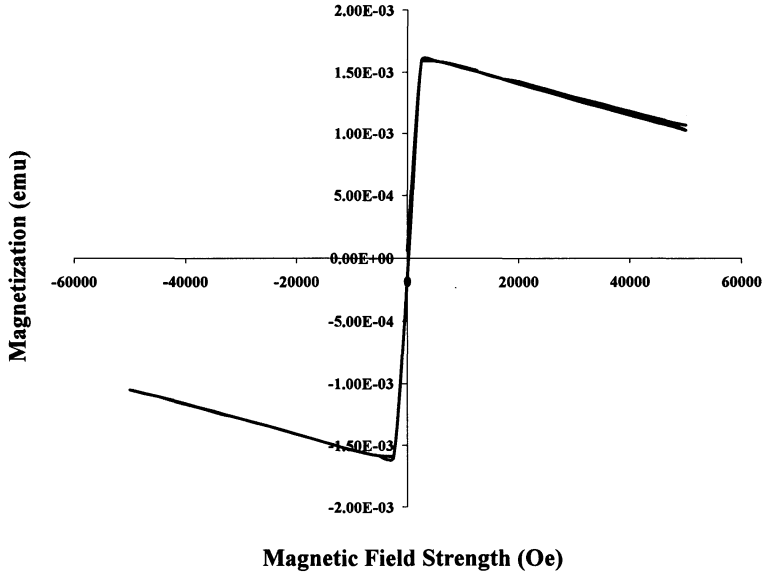

Figure 15. Magnetic characterization of GadoDex at 310 K, demonstrating superparamagnetism.

Once the stability of Gd^{3+}-ion clusters in GadoDex was confirmed, the sample was characterized by AFM and TEM. The AFM image of GadoDex showed a thickness of about 16-20 nm and a length of about 120 nm (**Figure 16**). The length of GadoDex is longer than the expected length of GNT alone (20-80 nm). This difference in the length can be attributed to the flattening of the AFM sample on the mica stub. The TEM image of the sample showed a similar thickness of 20 nm (**Figure 17**). The microscopy images

confirmed the presence of a single GNT or very small aggregate (2-3 tubes) of GNTs in each of the GadoDex entity.

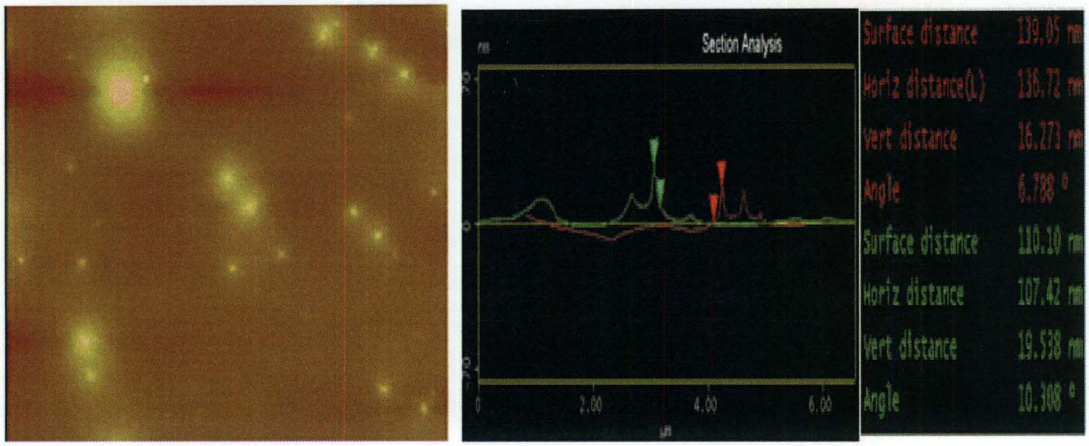

Figure 16. AFM image of a GadoDex sample with its section analysis.

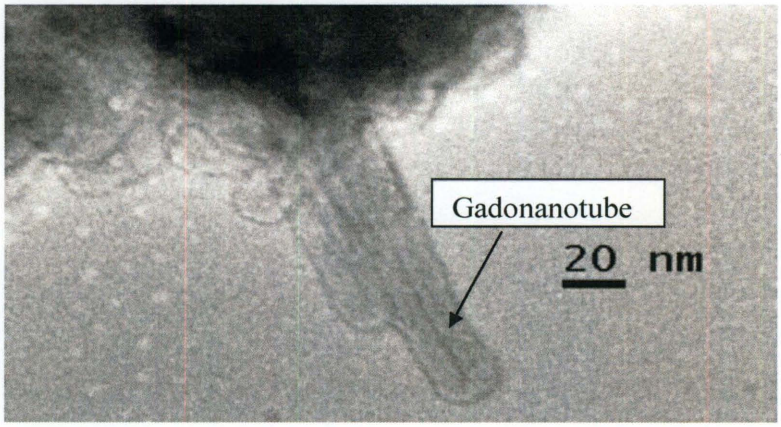

Figure 17. TEM image of GadoDex.

GadoDex exhibited a high degree of dispersibility in water (> 14.5 mg/mL). Due to the larger molecular weight of dextran (9,000-11,000 Da), the value may not necessarily translate into greater dispersity for GNTs. Thermogravimetric analysis (TGA)

of GadoDex showed that nearly 70% (w/w) of GadoDex is composed of carboxylated dextran (**Figure 18**). Using TGA and UV-Vis data, it can be estimated that the carboxylated-dextran coating resulted in the dispersion of 4.4 mg/mL of GNTs in water. This value is comparable to the dispersibility of SWNTs by SDBS (3.6 mg/mL),[37] demonstrating the superior dispersion ability of carboxylated-dextran. Thus, the benign pharmacological properties of the dextran coating provide an effective and biocompatible dispersion medium for GNT MRI CAs

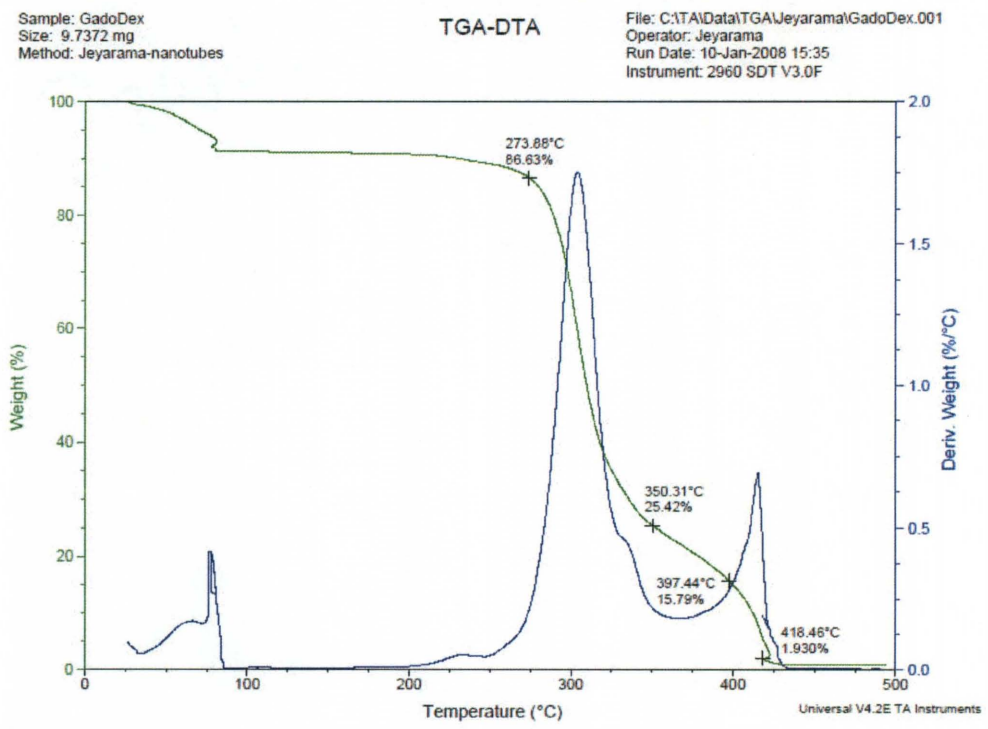

Figure 18. Thermogravimetric analysis for GadoDex.

MRI Relaxation Properties of GadoDex

Once a stable dispersion of GadoDex in water was obtained, the proton relaxation property of the sample was characterized. The relaxivity measurements were performed using a bench-top relaxometer at 60 MHz and 37 °C, and an inversion recovery pulse sequence was used to measure the longitudinal relaxation time (T_1). The longitudinal relaxivity (r_1) values of GadoDex and individual GNTs dispersed in sodium dodecyl benzene sulfonate (SDBS) surfactant are presented in **Table III**. Both of the GNTs exhibited similar relaxivities. When compared to Magnevist®, the GNTs are ~20 times more efficacious. In order to verify the bench-top relaxometer results with a clinical scanner, GadoDex was tested in a 3 T scanner, along with Magnevist®. The results from the clinical scanner also confirmed the superior efficacy of GadoDex over Magnevist® (**Figure 19**).

Table III. Comparison of longitudinal relaxivities for GNTs and Magnevist®. Measurements were performed at 60 MHz and 37 °C.

Sample	Relaxivity ($mM^{-1}s^{-1}$) per Gd^{3+} ion
Bundled GNT (SDBS-coated)	173
Individual GNT (SDBS-coated)	77.0
GadoDex	74.7
$[Gd(H_2O)_8]^{3+}$	8.4
Magnevist®	3.7

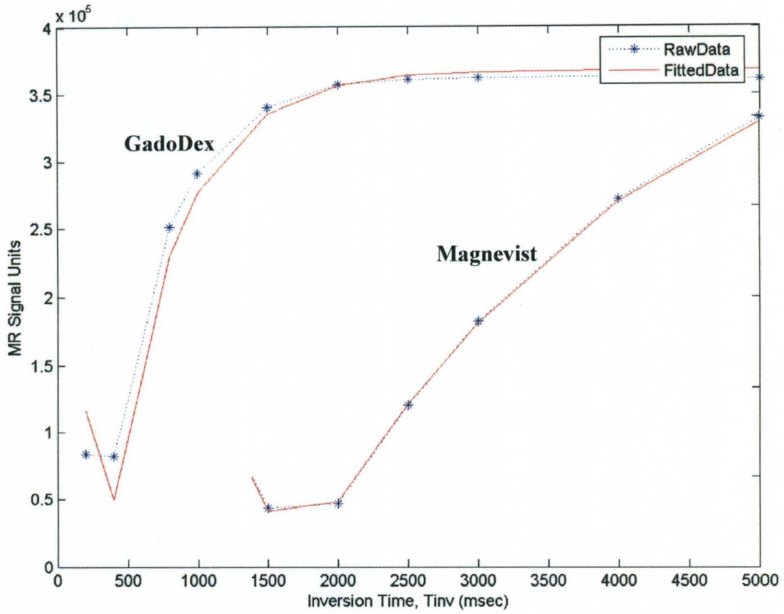

Figure 19. Inversion recovery graphs of GadoDex and Magnevist® (both at [Gd^{3+}] = 0.038 mM) in a clinical 3 T scanner.

Understanding the NMRD Profile for GadoDex

We now know that GadoDex has promising properties as an MRI CA and is more efficacious than current Gd-chelates. However, it is important to understand the parameters affecting the relaxivity of GadoDex to optimize their performance further. Measuring the relaxivity of a CA as a function of magnetic field (Nuclear Magnetic Relaxation Dispersion (NMRD)) is a valuable tool for the separation of different interaction mechanisms and dynamic processes affecting the relaxation behavior.[32] Thus, the NMRD profile for aqueous solution of GadoDex was recorded at 37 °C (**Figure 20**).

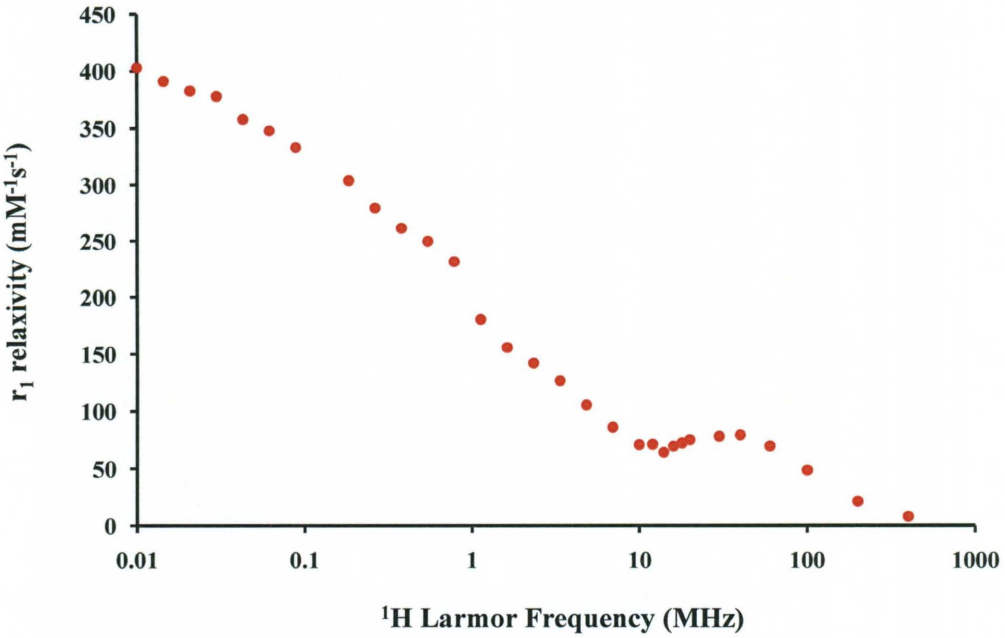

Figure 20. Nuclear magnetic relaxation dispersion (NMRD) profile for GadoDex at 37 °C.

The shape of the NMRD profile of GadoDex resembled that of bundled GNTs but with lower relaxivity at all field strengths. Due to the very high relaxivities at low-field strengths and the shape of curve at low-fields for GadoDex, the entire profile cannot be fitted by the standard Solomon-Bloembergen-Morgan (SBM) theory for proton relaxation by Gd-based CAs. However, the theoretical predictions using SBM theory can quite accurately reproduce the experimental NMRD profile in the medium-to-high field regime (ν_I > 10 MHz), which is the clinically-relevant range (**Figure 21**).

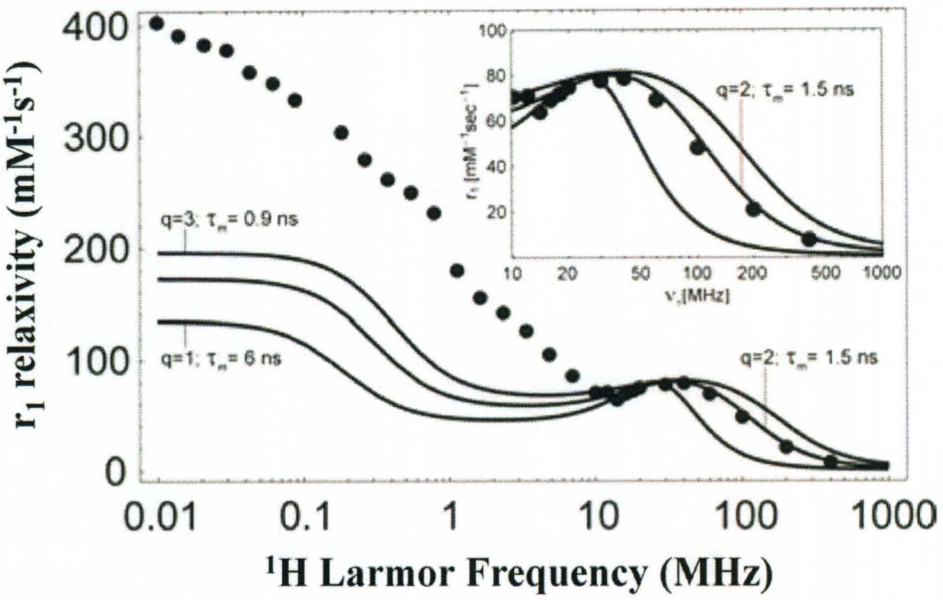

Figure 21. Theoretical fitting of the NMRD profile for GadoDex.

If it is assumed that the inner-sphere contribution to r_1 relaxivity dominates the outer-sphere contribution ($r_1^{OS} / r_1^{IS} < 1$) for GadoDex, as is the case for slowly rotating CAs with large relaxivity,[45] the fitting of the NMRD profile depends on the number of inner-sphere water molecules (q), the molecular tumbling time of the Gd-CA with the inner-sphere water molecules (τ_R), the proton exchange rate (τ_m), and the Gd^{3+} ion-water proton bond distance (r_{Gd-H}). Using this assumption, the best fit was obtained for q = 2, τ_R = 100 ns, τ_m = 1.5 ns, r_{GdH} = 0.31 nm, with the values for other parameters as listed in the **Table IV**. The accuracy of the fitting is clearly shown in the inset of **Figure 21**.

Table IV. Various parameters used for fitting the NMRD profile of GadoDex.

Parameter	Value
q	2
τ_R	100 ns
τ_m	1.5 ns
r_{Gd-H}	0.31 nm
τ_v	10 ps
Δ^2	5×10^{18} s^{-2}

The characteristic τ_R value used for the fitting is considerably longer when compared to general Gd-polyaminocarboxylate CAs so far studied (**Table V**). However, this τ_R value is not unreasonable, given that for a spherical CA of radius a = 5 nm tumbling in aqueous solution, the characteristic τ_R is about 100 ns, and larger values can be estimated for a cylindrical nanoparticle (GadoDex is ~100 nm long and 20 nm in diameter). As regarding the other fitting parameters (except for q, τ_R and τ_m as discussed above), their values fall within the ranges normally observed for Gd-based CAs. When compared to traditional Gd-chelates, a significant difference for GadoDex is observed for both the molecular tumbling time (τ_R) and the proton-exchange rate (τ_m) (**Table V**). Both of these parameters are certainly due to the US-tube component of GadoDex, reiterating their importance in MRI relaxation of GadoDex. However, it is surprising that q = 2 is so low for GadoDex, since the potential coordination number for the naked Gd^{3+} ions within GNTs is 8-9. Some of the coordination sites might be occupied by possible hydroxyl bridges between Gd^{3+} ions in the GNTs (and are probably responsible for maintaining the

Gd^{3+}-ion clusters even when physiologically challenged). In addition, the hydrophobic inner surface of US-tubes might prevent the access of water protons to certain coordination sites. In spite of these possibilities, a greater number (4-6) of inner-sphere water molecules (q) was expected for GadoDex to account for their superior relaxivity. It is presently believed that the lower value of q = 2 from NMRD profile fitting, is likely due to the coordination of the carboxyl groups of dextran with Gd^{3+} ion clusters. Thus, one of the possible ways to improve the relaxivity of GadoDex further would be to covalently functionalize the US-tube surface with dextran, thereby increasing the number Gd^{3+}-ion coordination sites available for proton exchange.

Table V. Comparison of parameters from fitting NMRD profiles for various Gd-based MRI CAs.

Compound	τ_R	τ_m	q	r_1 ($mM^{-1}s^{-1}$) per Gd^{3+} ion
Magnevist®	54 ps	143 ns	1	3.4
Dotarem®	53 ps	122 ns	1-2	3.1
$[Gd(H_2O)_8]^{3+}$	-	1.2 ns	8-9	8.4
Gadonanotubes	100 ns	1.5 ns	2	~ 100

Interestingly, the r_1 relaxivities of individual GNTs (regardless of the nature of the surfactant) dropped by ca. 50 % when compared to bundled GNTs (**Table III**). The observed decrease in longitudinal relaxivity can be attributed to the debundling procedure. As we have seen above, the longitudinal relaxivity of GNTs is determined by

the number of inner-sphere water molecules (q), the molecular tumbling time of the CA (τ_R), and the proton exchange rate (τ_m) of inner-sphere water molecules of the CA with bulk water molecules. Debundling of GNT aggregates by the Na^0/THF method results in lower molecular-weight individual GNTs which might tumble faster than higher molecular-weight bundled GNTs. In addition, water molecules can get trapped in the interstices of the GNT aggregates, leading to a different diffusion rate and proton exchange rate. Such aggregate-dependent relaxation enhancement mechanisms have previously been reported for gadofullerenes.[46] Another significant difference between bundled GNTs and GadoDex is the fall-off of relaxivity at higher field strengths (to only 21 $mM^{-1}s^{-1}$ at 4.7 T) for GadoDex, whereas, the relaxivity of bundled GNTs plateaus at field strengths above 1.41 T. This phenomenon cannot be explained with current results and will require carefully designed studies to understand in detail. Also, the lack of stability of GadoDex in phosphate-buffered saline (PBS) (visible precipitation in 1 hour) needs to be overcome for long-term *in vivo* and molecular imaging studies. Possibly, the lack of stability in PBS of GadoDex (due to the weak interaction between the Gd^{3+}- ion cluster and carboxylated dextran) can be overcome by covalently attaching the dextran component to the GNT sidewalls.

CONCLUSION

In summary, we have developed a biocompatible carboxylated-dextran coating for the dispersion of GNTs. The carboxylate groups of dextran likely forms a weak bonding interaction with the Gd^{3+}-ion clusters available at the defect sites of GNTs to provide dispersibility. The aqueous dispersibility of GadoDex (4.4 mg/mL) is comparable to that of SDBS-coated SWNTs. GadoDex retains the superior contrast enhancement efficacy of

GNTs and exhibits greater relaxivities at all field strengths compared to commercially-available Gd-based agents. Their very high relaxivities at low-field strengths make GadoDex an attractive candidate for low-field MRI. The theoretical fitting of the NMRD profile of GadoDex attributes the observed high relaxivities to the synergistic effect of increased τ_R and τ_m when compared to Gd-chelate CAs. The fitting of the NMRD profile also demonstrates the important role played by the US-tube component of GadoDex. The relaxivity may further be enhanced for GadoDex by covalently functionalizing the external surface of GNTs with dextran, thereby increasing the number of inner-sphere water molecules in the Gd^{3+}-ion clusters.

CHAPTER 4

Part A: Gadonanotubes as T_2-weighted MRI CAs

Brief Introduction to T_2-weighted MR Imaging

Contrast agents for MRI are classified into two categories: 1) CAs that shorten the spin-lattice relaxation rates of water protons (T_1-weighted CAs) and 2) CAs that shorten the spin-spin relaxation rates (T_2-weigthed CAs). The T_1-mechanism involves interaction (direct and indirect) with the surrounding protons. Hence, most of the T_1-weighted CAs (mainly Gd-complexes) have direct exchange with the water protons in its vicinity (**Figure 3**). The T_2-mechanism is more dependent on the magnetic properties of the CAs than on their proton exchange properties. Both T_1-weighted and T_2-weighted proton relaxation require respective CAs to have magnetic properties, hence, a T_1-weigthed CA will have T_2-shortening properties and vice versa. A CA is labeled as a T_1-weighted CA or a T_2-weighted agent based on the dominant effect (relaxivity; $r_{1,2}$) of one of the two mechanisms. If $r_2/r_1 \leq 2$, then the agent will be a T_1-weigthed CA; if $r_2/r_1 > 2$, then the agent acts as a T_2-weighted CA.[32]

GNTs have shown contrast enhancement efficacy at least 40 times better than current clinically-used Gd-based CAs such as Magnevist® (**Table III**) at a clinically relevant field strength of 1.41 T. Their T_1-contrast enhancement is due to the presence of encapsulated Gd^{3+}-ion clusters in the hollow interior of the US-tubes. However, their superparamagnetic nature (**Figure 22**) suggests that they can also act as T_2-weighted CAs. In this chapter, we discuss the possibility of GNTs to act as T_2-weighted MRI CAs

at higher magnetic field strengths and their use as labeling agents for cellular and molecular imaging.

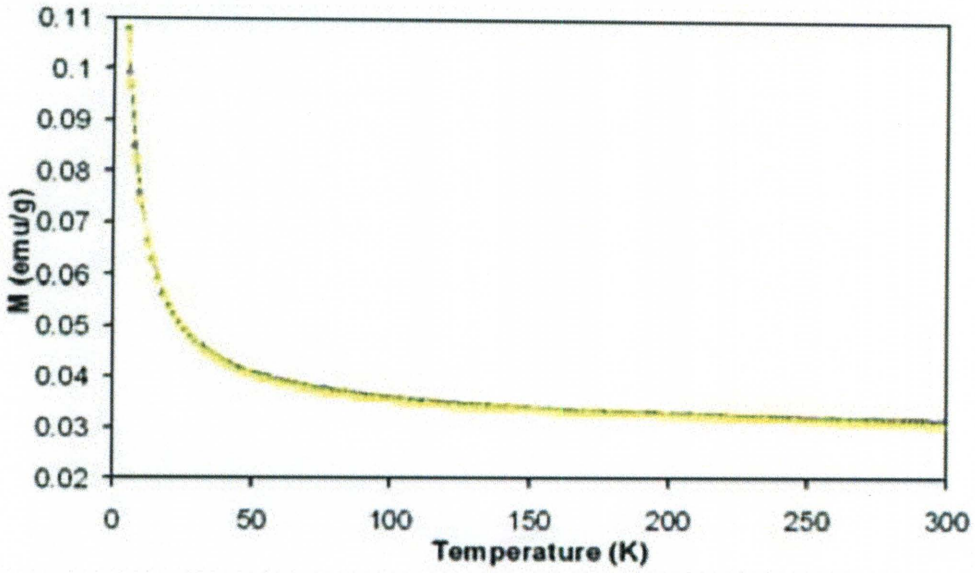

Figure 22. Zero-field-cooled and field-cooled (ZFC+FC) curve for GNTs demonstrating their superparamagnetism. Reproduced with permission Ref. 18.

MATERIALS AND METHODS

Relaxometry Measurements

Individual GNTs were synthesized using the procedure detailed in Chapter 2. The T_2-proton relaxation studies were performed on a Bruker Minispec mq series (30, 40, and 60 MHz) and on Bruker NMR spectrometers (100, 200, and 400 MHz) using Carr-Purcell-Meiboom-Gill (CPMG) sequence. Relaxivity measurements were also performed in a clinical 3 T MRI system (General electric, Milwaukee, WI). The transverse relaxivities (r_2) of the samples were measured by a Hahn spin-echo sequence with TR =

500 ms, TE = 10 ms, 11ms, 12 ms, 13 ms, 14 ms, 15 ms, 25 ms, 50 ms, 75 ms, and 100 ms. T_2 of each phantom was obtained by linear fitting of $\log(S) = \log(S_0) - TE / T_2$.

RESULTS AND DISCUSSION

Transverse Relaxation Properties of Gadonanotubes

The transverse relaxation rates (R_2) of GNTs at different proton Larmor frequencies are presented in **Table VI**. The transverse relaxation time (T_2; as a result R_2) are dependent on the concentration of the CA. In order to compare GNTs with other T_2-weighted MRI CAs, it is necessary to compare their relaxivity, which is normalized for concentration. The transverse relaxivity (r_2) of GNTs are calculated as a function of Gd^{3+} concentration and is also presented in **Table VI.**

Table VI. Transverse relaxivities (r_2) of GNTs at different proton Larmor frequencies. Measurements were performed at 37 °C.

Larmor frequency (MHz)	Relaxation Rate (s^{-1})	[Gd^{3+}] mM	Relaxivity (r_2) $mM^{-1}s^{-1}$ per Gd^{3+} ion
30	14.27	0.035	403
40	15.32	0.035	434
60	15.68	0.035	444
100	14.71	0.035	416
200	14.49	0.035	410

GNTs showed exceptionally large transverse relaxivities at all field strengths. When the transverse relaxivity (r_2) of GNTs is compared to their longitudinal relaxivity (r_1) at a clinically-relevant field strength of 1.41 T, the data indicates that GNTs are strong T_2-weighted MRI CAs (**Table VII**). For comparison, relaxivity for a clinically-

used iron oxide-based MRI CA (for T_2-weighted imaging),[47] and a Gd-based agent (for T_1-weighted imaging)[10] are also presented in **Table VII**. GNTs far outperform Ferumoxtran® in their transverse relaxivity and Magnevist® in their longitudinal relaxivity.

Table VII. r_2/r_1 ratio for GNTs at 1.5 T and 37 °C. For comparsion, relaxivity values for clinically-used Magnevist® and Ferumoxtran® are also presented.

Sample	r_1 relaxivity ($mM^{-1}s^{-1}$) per Gd^{3+} ion	r_2 relaxivity ($mM^{-1}s^{-1}$) per Gd^{3+} ion	r_2/r_1
Magnevist®	3.4	4.5	1.3
Gadonanotubes	97	444	4.6
Ferumoxtran®	10 (based on [Fe])	65 (based on [Fe])	6.5

To confirm that the observed exceptionally large transverse relaxivity of GNTs can be reproduced in a clinical scanner, we tested GNTs in a high-field (3 T) clinical scanner. GNTs retained the high transverse relaxivity in a clinical scanner (424 $mM^{-1}s^{-1}$). However, as observed in the NMRD profile of GadoDex (**Figure 20**), their longitudinal relaxivity (68 $mM^{-1}s^{-1}$) is significantly lower than at 1.5 T (97 $mM^{-1}s^{-1}$). The reduction in longitudinal relaxivity further increases the r_2/r_1 ratio (from 4.58 at 1.5 T to 6.5 at 3 T), making GNTs an attractive candidate for cellular and molecular imaging using T_2-weighted MRI at higher magnetic field strengths. This is counterpoint to our longstanding belief that GNTs are superior T_1-weighted CAs at low fields (mT to 3 T) and a high-performance T_2-weighted CAs at higher field strength (> 3 T). In order to better understand the transverse relaxivity of GNTs, we performed a control of US-tubes alone (with no Gd^{3+} ions). Previously, it was reported that the US-tubes alone do not have an

appreciable T_1-relaxation property.[18] However, T_2-relaxation measurements showed that US-tubes are excellent T_2-weighted CAs, even in the absence of any Gd^{3+} ions. The T_2-shortening properties of the empty US-tubes can be attributed to the metal catalyst particles (Y, Ni in arc-discharge tubes) used in the synthesis of SWNTs. Even though the cutting process removes the majority of the catalyst, some of it still remain with the US-tubes (ca. 2% Ni & 0.6% Y) and there are other metal catalyst impurities like iron (< 0.1%) also present. These metal catalyst particles have inherent magnetic properties, thus producing transverse relaxation for empty US-tubes. Since most of these metal particles are likely buried under a hydrophobic carbon sheath, they have little or no interaction with water protons. This likely explains the absence of any longitudinal relaxivity (T_1-relaxation) for empty US-tubes. With these results in hand, the r_2/r_1 values presented in **Table VII** may not reflect the actual relaxation behavior for GNTs.

Delineating the contribution from Gd^{3+} ions on the transverse relaxation rate (T_2-relaxation) of GNTs is complicated by the lack of data about the molecular weight of the US-tubes. However, the amount of US-tubes present in a stable GNT suspension used for the relaxivity measurements can be calculated using the metal catalyst and Gd^{3+} ion concentration. Using this method, a solution was prepared with empty US-tubes having the same amount of US-tubes as in GNT solution. In order to make a homogenous solution, known quantities of each of the two samples (US-tubes and GNTs) in the absence of surfactant were analyzed for their metal catalyst (Ni, Y, Fe & Gd) content by ICP-OES. The ICP measurements (agreement within 2%) were run in triplicate to determine the average metal content in each sample. Then the two samples dispersed in Pluronic® surfactant were analyzed for their metal content, and, from these values, the

amount of US-tubes present in each of the sample was determined. The US-tube sample was then diluted such that the concentration of US-tubes in both the sample was the same. The T_2-relaxation time of both the samples were measured in a bench-top relaxometer (60 MHz; 37 °C). The T_2-relaxation time of empty US-tube sample was subtracted from that of GNTs. The difference in relaxation times between the two samples was attributed to the actual transverse relaxation effect from Gd^{3+} ions (**Table VIII**).

Table VIII. Delineating the contribution of Gd^{3+} ion on the relaxivity of GNTs. Measurements were performed at 60 MHz and 37 °C.

Sample	Concentration (mg/L)	T_2 (ms)	r_2 ($mM^{-1}s^{-1}$) per Gd^{3+} ion	r_2/r_1 based on [Gd^{3+}]
US-tubes	164.6	270	-	-
GNTs	172 [Gd^{3+}]=0.047 mM	127	117	1.2
Magnevist®	-	-	4.5	1.3

Our method for determining the contribution from Gd^{3+} ion may not be the ideal procedure, since the presence of paramagnetic Gd^{3+} ions inside the US-tubes might lead to magnetic coupling between the metal catalyst particles and Gd^{3+} ions. Any such coupling might have a profound impact on the transverse relaxation mechanism of GNTs. However, until a complete magnetic characterization of empty US-tubes and individual contribution from each of the metal catalyst particles are completely understood, the present method provides the best available analysis.

Part B: Cellular Uptake and Single-Cell Imaging using Gadonanotubes

The inherent optical properties of SWNTs have been utilized to track them by various imaging modalities. For example, *in vitro* imaging of SWNTs in cells and *ex vivo* imaging in animal tissue have been demonstrated using near-infrared (NIR) fluorescence imaging,[38, 48] Raman spectroscopy,[49] and x-ray fluorescence microscopy.[50] In addition, several agents such as iodine,[16] fluorescing molecules,[51] iron oxide,[52] or radiotracers[53] have been attached either to SWNT surfaces or encapsulated within their hollow interiors for imaging. By and large, optical microscopy remains the most popular imaging modality for visualization of SWNTs in cells and tissue. In general, however, optical imaging suffers from low tissue penetration. In most cases, evaluation of SWNT delivery by optical imaging can only be confirmed by *in vitro* experiments or by examining *ex vivo* tissue samples, and the samples often require proper staining for better visualization.[54]

Introduction to Cellular Imaging Using T_2-weighted MRI

In order to track SWNT-based drug delivery platforms *in vivo* and follow their post-treatment biodistribution and their ultimate biological fate, real-time visualization and quantification of the SWNT core itself is desirable. Among various diagnostic imaging modalities, MRI offers the advantages of non-ionizing, non-invasive, multi-planar capabilities that favor the long-term tracking of SWNT materials *in vivo*. Currently, molecular and cellular imaging using MRI mostly revolves around the use of iron oxide-based r_2 agents, such as superparamagnetic iron oxide nanoparticles (SPIOs) or micron-sized iron oxide particles (MPIOs).[29, 30, 44] In the preceding part of this

Chapter, we have shown that GNTs are high-performance r_1 and r_2 MRI CAs. They are also a more efficient T_2-relaxation agent than SPIOs already in clinical use (**Table VII**). In fact, subcutaneous injection of GNTs dispersed in a biocompatible surfactant (Pluronic® F-127) has recently shown excellent negative contrast (T_2-shortening) *in vivo* for the first time.[55]

In this part of the Chapter, the intracellular uptake of the GNTs and a method (R_2 & R_2* mapping *in vitro*) to quantify the intracellular uptake for GNTs will be discussed. Quantifying the changes in R_2 and R_2* of the cells by known amount of GNTs (quantitative R_2 and R_2* mappings) allows a method to estimate the cellular uptake of GNTs in a non-invasive fashion. The resourcefulness of our method was tested *in vivo* with subcutaneously injected GNT-labeled cells in a mouse. The ability of GNTs to act as a high-performance T_2-weigthed MRI CAs as the first non-iron oxide-based T_2 weighted CA with the potential to image single cell *in vitro* is considered below in this part of the Chapter.

MATERIALS AND METHODS

For MRI measurements and intracellular uptake studies, a stable solution of individual GNT was required. A stable and biocompatible GNT suspension was prepared by dispersing 10 mg of individual GNTs in 10 mL of 1.0% (w/v) Pluronic® F108 solution using a probe sonicator. The resulting suspension was centrifuged at 3200 rpm for 15 minutes to remove any large aggregates. The supernatant was collected and dialyzed (50,000 MW cut-off membrane) against running water for 3 days to remove excess surfactant. The Gd^{3+}-ion concentration of GNT suspension was determined using

inductively-coupled plasma optical emission spectrometry (ICP-OES, Perkin-Elmer Optima 3200V), giving a final concentration of 111 μM Gd.

Cell Culture and GNT Labeling

A J774 mouse macrophages cell line (ATCC, Manassas, VA) was cultured at 37 °C and 5% CO_2 in 100 x 20 mm tissue culture dishes using standard cell culture media, containing Dulbecco's Modified Eagle Medium (DMEM, Invitrogen) with 10% fetal bovine serum (FBS, Invitrogen) and 1% Penicillin-Streptomycin (S/P, Fisher Scientific). *In vitro* cytotoxicity of GNTs was first tested in a 96-well micro-plate using a MTS-based cell proliferation assay (CellTiter 96® Aqueous One Solution Assay, Promega). To optimize the concentration of GNTs that can be used for efficient cell labeling, four different concentrations (37.0, 27.75, 15.86, and 12.33 μM Gd) were tested, using unlabeled cells as a control. Each concentration was tested in triplicate.

For cell labeling experiments, 5×10^5 cells/well were plated in 6-well plates for 24 hours to allow cell adhesion. The cells were then incubated with GNT suspension diluted with the standard culture media (final $[Gd^{3+}]$ = 27.75 μM) for 24 hours. The labeled cells were then washed twice with phosphate-buffered saline (PBS, Invitrogen) to remove any excess GNTs that might be adsorbed on the cell membrane.

Fluorescence Staining and Microscopy

To visualize the sub-cellular localization of GNTs, the labeled cells were stained with blue fluorescent Hoechst dye (Invitrogen). Hoechst dye is a cell-permeable nucleic acid stain that increases fluorescence intensity when bound to DNA and is commonly

used to locate nuclei in cells. The labeled cells were incubated with the dye in culture media for about 15 minutes and then examined with fluorescence microscopy (Olympus IX51). Bright-field microscopic images were also captured for the same cell samples, to observe the localization of GNTs within the cell, as well as to identify the location of the cell nuclei.

In vitro MRI Phantom Preparation

For *in vitro* MRI experiments, a portion of the labeled cells was re-suspended in an equal volume of 2× DMEM culture media and 2 % agarose gel (Type VII, Sigma) at 37 °C and transferred to 1 cc syringes for MRI phantom studies. The process was performed carefully to avoid air bubbles inside the 1 cc syringes and premature gelling of the agarose mixture. Four different concentrations of homogeneously-dispersed labeled cell phantoms (2.3×10^6, 1.5×10^6, 0.75×10^6, and 0.57×10^6 cells/ml) were prepared for relaxivity measurements at 3 T. Four phantoms at the same concentration of unlabeled cells were also prepared as controls. In addition, a sparsely-distributed labeled cell phantom (5,500 cells/mL) was also prepared for single-cell visualization studies at high field MRI (9.4 T). All phantoms were cylindrical in shape and about 3.5 cm long.

The concentration of Gd^{3+} ions in each of the phantoms was determined by ICP-OES. From the concentration of Gd^{3+} ions and the total number of cells, the average uptake of Gd^{3+} ion by each cell was calculated. The measurements were performed in triplicate and the mean and standard deviations of the results were also calculated.

Animal Preparation

For *in vivo* relaxometry measurements, a portion of the GNT-labeled cells were suspended in PBS and mixed with 1% agarose gel at 37 °C for subcutaneous injection into the dorsal flank of a female C57BL/6 mouse (Charles River, Wilmington, MA). A total of 4×10^5 labeled cells/pellet with a volume of 50 μL was injected into the left dorsal flank of the mouse. The injection was done carefully to create an inflated bulb for easy localization by MRI. An equivalent unlabeled cell pellet (4×10^5 cells) in 1 % agarose gel was also injected into the right side of the dorsal flank as a control. The animal was then immediately transferred to a 3 T MRI instrument for imaging. The animal experiment was approved by the Institutional Animal Care and Use Committee of The Methodist Hospital Research Institute.

MRI Measurements

MRI was performed in a whole-body 3 T system (General Electric, Milwaukee, WI) using a 35 mm inner diameter custom-built quadrature coil for *in vitro* and *in vivo* relaxivity measurements and in a 9.4 T system (Bruker Biospec 94/20 USR) for the single-cell imaging experiment.

For *in vitro* relaxivities studies at 3 T, the 1 cc syringes were positioned at the iso-center of the magnetic bore, with the cylindrical axis parallel to the main B_0 field. R_1 relaxation of the GNT solution was measured using a 2D spin-echo inversion recovery (IR) sequence with the following imaging parameters: TR/TE=5000/15 ms, IR = 60 - 150 ms with 10 ms increment and 200 - 800 ms with 100 ms increment, FOV = 5.0 cm,

matrix = 128 × 128, NEX = 1, thickness = 1 mm, no. of slice = 4. R_2 and R_2* relaxations of the solution were also measured using 2D spin-echo and gradient echo sequences respectively, with TR = 1500 ms, TE = 10-45 ms with 5 ms of increment, FOV = 5.0 cm, matrix = 192×192, NEX = 1. Circular ROIs were drawn and the R_1, R_2 and R_2* relaxations of the phantoms were computed using non-linear curve fittings of the mean intensity of each ROI in the images using Matlab (Mathworks™, Natick, MA). For the GNT-labeled and unlabeled cells phantoms, the R_1, R_2, and R_2* relaxations were measured and computed with similar imaging parameters but using a different range of IRs (50-2500 ms) for R_1 and TEs (15-125 ms with 15 ms increment) for R_2 and R_2*. The net relaxations, ΔR_2 and ΔR_2*, of the labeled-cell phantoms were calculated by subtracting the R_2 and R_2* values of the unlabeled-cell phantom controls from the measured R_2 and R_2^* values of the labeled-cell phantoms.

For *in vivo* relaxometry measurement at 3 T, images were acquired by cutting a high-resolution oblique slice covering the injected cell pellets on both sides of the mouse, with imaging parameters: TR = 1500 ms, TE = 10-45 ms with 5 ms of increment, FOV = 6.0 cm, matrix = 256×256, NEX = 1. The images obtained were then realigned using SPM2 to reduce motion artifacts and fitted mono-exponentially for R_2* mapping using Matlab. ROIs were drawn at the two pellets for the R_2* maps and overlaid onto an anatomical image. The coefficient of determination (R^2) map was also computed.

For single-cell visualization, the sparsely-distributed labeled-cell phantom (5,500 cells/mL) was imaged at 9.4 T using a 3D spoiled gradient echo sequence (TR/TE = 3000/40 ms, alpha = 28.6°, FOV = 0.64×2.56 cm, resolution = 50 μm isotropic, NEX =

12). The cylindrical axis of the phantom was placed parallel to the main B_0 field. Reconstruction was done using the susceptibility-weighted imaging (SWI) method, by multiplying the phase mask with the original magnitude image to enhance the contrast effect for better visualization.[56]

RESULTS AND DISCUSSION

The relaxivity of the GNT suspension was characterized prior to cell labeling in a 3 T scanner. The relaxation rates (R_1, R_2 & R_2*) of GNT in a 3 T magnetic field is given in **Table IX**. GNT suspension showed an R_1 relaxation of 7.50 s^{-1}, which was equivalent to a relaxivity (r_1) of 67.57 $mM^{-1}s^{-1}$ (per Gd^{3+} ion). R_2 and R_2* relaxation rates were 47.04 s^{-1} and 49.88 s^{-1}, respectively. All the fitted curves had R^2 values close to 1, indicating an excellent fit of the measured data.

Table IX. Relaxation rates of the GNT solution at 3 T. The coefficient of determination (R^2) of each measurement is also shown.

Sample	Relaxation rate (s^{-1})		
	R_1 (R^2)	R_2 (R^2)	R_2* (R^2)
Gadonanotube	7.50 (0.98)	47.04 (0.99)	49.88 (0.99)

Cell Viability Studies for GNTs

For any cell labeling and imaging studies, it is necessary to optimize the labeling concentration of the agent to avoid any adverse effects to the cell. To determine the optimum concentration of GNTs that can be used for labeling cells without apparent cytotoxicity, we tested four different concentrations of GNTs (37.0, 27.75, 15.86, and

12.33 μM Gd) in a murine macrophage cell line (J774). The cell viability was tested using the MTS (3-(4,5-dimethylthiazol-2-yl)-5-(3-carboxymethoxyphenyl)-2-(4-sulfophenyl)-2H-tetrazolium bromide) assay. The MTS assay is a widely-used colorimetric method to assess cell proliferation and cytotoxicity of biomaterials. In viable (living) cells, the reductase enzymes reduce the MTS dye to Formazan dye giving a purple color. **Figure 23** represents the cell viabilities of the four different concentrations of GNTs tested. When the GNT concentrations are ≤ 28 μM Gd^{3+} the cells exhibited no observable toxicity. However, when the labeling concentration was increased to 37 μM Gd^{3+}, significant cell death occurred (~ 20 % of the cells). Hence, for the rest of the labeling studies we used 28 μM Gd as the labeling concentration.

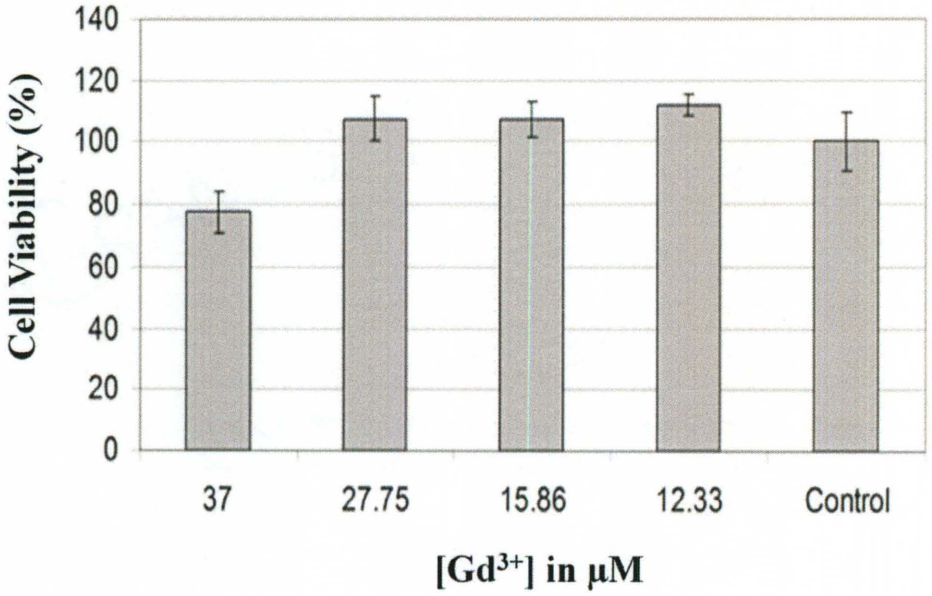

Figure 23. Cell viability studies using an MTS assay. For each concentration, the measurements were performed in triplicate and the mean ± standard deviation is shown.

Cell viability studies showed that at 28 μM Gd^{3+}, GNTs are non-cytotoxic to macrophage cells. However, they do not reveal whether the labeling agent (GNTs) was taken up by the cells or just at the periphery of the cell membrane. To visualize the uptake and localization of GNTs by macrophages, we used bright-field and fluorescent microscopy. **Figure 24a** is the bright-field image of GNT-labeled cell (at 28 μM Gd^{3+}) and **Figure 24b** is the corresponding blue-fluorescent image using Hoechst dye at the same cell spot.

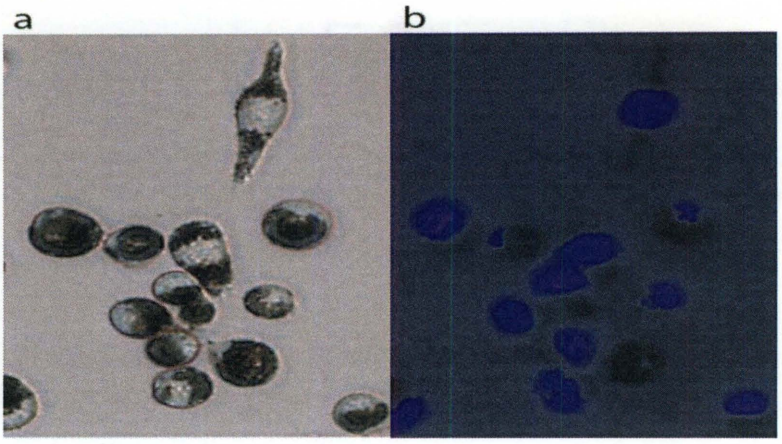

Figure 24. Microscopy images of GNT-labeled macrophage cells (a) Bright-field image of cells labeled with 28 μM Gd^{3+} (b) Blue fluorescence image of the labeled cells, captured at identical cell positions as in the bright-field image.

Figure 24 confirmed the presence of GNTs in the intracellular space. The GNT-labeled cells appeared black in the intracellular space under bright-field microscopy (**Figure 24a**). To determine whether the GNTs were able to penetrate the nucleus of the cells, we used nucleus-staining Hoechst dye. The blue fluorescent microscopy image

(**Figure 24b**) revealed the GNTs are unable to penetrate the cell nuclei under the conditions used. From the microscopy images it is clear that the GNTs accumulated mostly in the cytoplasm, without penetrating into the nucleus. The Hoechst dye also serves as a secondary live/dead assay, since only the nuclei of living cells can be stained. The MTS assay and the microscopy results confirm that the GNTs (28 μM Gd^{3+}) can efficiently label cytoplasm without any adverse effects in macrophage cells. We also analyzed the concentration of GNTs inside the labeled cells using ICP-OES. The ICP results indicated an average cellular uptake of 0.44±0.09 pg Gd^{3+}/cell, corresponding to an uptake of 19.3±3.8 pg GNTs/cell (2.9 % Gd (w/w)).

In vitro MR imaging

To generate a method to quantify and track the GNTs (or potentially SWNTs) in real-time, we measured the change in relaxation rates (ΔR_1, ΔR_2, ΔR_2^*) of cells upon labeling them with GNTs. Unlabeled cells were used as controls. The measurements were done in a 3 T clinical scanner with increasing number of GNT-labeled cells. To avoid volume induced artifacts, we homogenously dispersed the labeled cells in 1 % agarose gel. Interestingly, we did not observe any change in the R_1 relaxation rate of cells upon labeling with GNTs. However, the cells showed a higher R_2 and R_2* relaxation rates upon labeling with GNTs. **Figure 25** shows the linear relationship of ΔR_2 and ΔR_2^* with increasing number of GNT-labeled cells. The Gd^{3+} concentration in each of the cell phantoms was measured using ICP-OES (**Figure 25b**). **Figure 25a and 25b** confirm that the observed change in the relaxation rate is due to the increasing concentration of GNTs in each of the cell phantom. ΔR_2 and ΔR_2^* in **Figure 25** represents the net change in

relaxation rates of labeled cells with the contributions from unlabeled control cells, 1 % agarose gel as well as field inhomogenities subtracted. For all the labeled cell concentration, the change in R_2^* (ΔR_2^*) is much higher than the change in R_2 (ΔR_2), suggesting that R_2^* is the dominant relaxation mechanism in GNT-labeled cells and R_2^* mapping can be used to quantify the cell population *in vivo*.

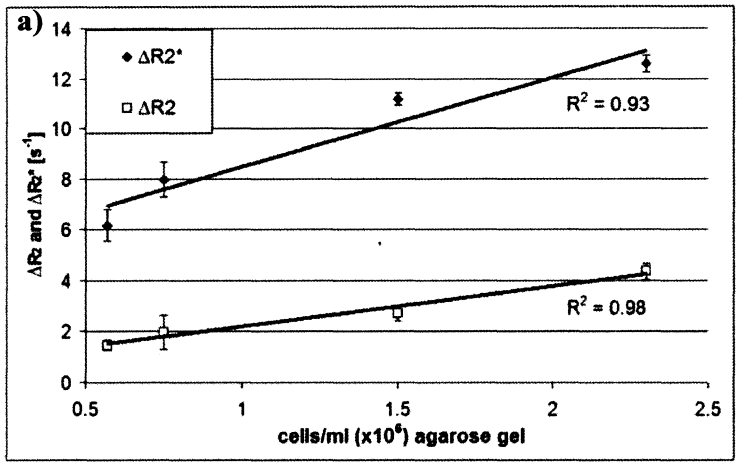

b)

Cells	$[Gd^{3+}]$ μg
2.3×10^6	0.85
1.5×10^6	0.61
0.75×10^6	0.43
0.57×10^6	0.25

Figure 25. (a) ΔR2 and ΔR2* relaxation measurements of the GNT-labeled cell phantoms with increasing number of labeled cells in 1.0 % agarose gel at 3 T. (b) The concentration of Gd^{3+} ions in the phantoms, as determined by ICP-OES.

It is interesting to note that all of the GNT-labeled macrophage cells, regardless of the $[Gd^{3+}]$, showed no R_1 enhancement upon labeling. However, the stock solution of GNTs used for labeling showed considerable R_1 relaxation (**Table IX**). We have also seen that when breast cancer cell line (MCF-7) was labeled with serine-derivatized GNTs, significant R_1 relaxation was observed.[57] The observed difference in R_1-enhancement between different GNT-labeled cell lines may be due to difference in the intracellular localization of GNTs in different cell line. It is not uncommon for the sub-cellular localization to affect the longitudinal relaxation of the CAs. It has been reported

that the R_1 relaxation is sensitive to the CA (Gd-complexes) internalization pathway. The entrapment of the CA in the intracellular vesicles through simple pinocytosis could result in a three-site water exchange compartmentalization, and the entrapment could slow down the water relaxation (decrease the relaxivity) when the CA concentration increases.[58]

The GNTs showed considerable difference in R_2 and R_2^* relaxation rates upon internalization in macrophage cell line. It is worth noting that R_2^* is only slightly greater (~ 6 %) than R_2 in the GNT stock solution (**Table IX**), however, the effect is more pronounced upon intracellular localization (3-4 times). The close packing of GNTs, once localized intracellularly, can induce susceptibility effects resulting in greater R_2 and R_2^* relaxation in labeled cells. A susceptibility-induced increase in transverse relaxation rates has been previously reported for cells labeled with superparamagnetic iron oxide particles.[33-35] Transverse relaxation rates are determined more by the magnetic properties of the CAs than the chemical nature of the agents. Hence, the superparamagnetic nature of GNTs suggests that their transverse relaxation mechanism upon cellular internalization could be similar to that of iron oxide nanoparticles.

In vivo Imaging and Quantification of Labeled-cell Population

To test the feasibility of using ΔR_2^* mapping for quantification of the labeled-cell population *in vivo*, we subcutaneously injected a known number of GNT-labeled cells (8×10^6 cells/mL in pellet form) into the left dorsal flank of the mice and imaged them in a clinical 3 T scanner. The labeled-cell pellets were substantially darker than the surrounding tissue, whereas, the unlabeled control cells showed negligible contrast

difference compared to the surrounding tissue (**Figure 26a**). This clearly demonstrates that the GNTs can be used for *in vivo* T_2-weighted MR imaging. The T_2^* of the labeled cells were estimated to be 16.83 ± 5.30 ms corresponding to an R_2^* value of 65.50 ± 21.80 s^{-1}. The unlabeled control cells have T_2^*= 40.58 ± 16.26 ms corresponding to an R_2^* value of 28.60 ± 11.6 s^{-1}. The labeled cells have R_2^* enhancement ~2.5 times greater than that of unlabeled control cells. The difference in the R_2^* relaxation rates (ΔR_2^*) between labeled and unlabeled cells is 36.90 s^{-1}. When this value was plotted in **Figure 25a** (by extrapolating the linear regression line), it fits well with the data generated using other labeled cell concentration (**Figure 25a**) and the estimated cell population (8.3×10^6 cells) is very close to the actual cell population used for the studies (8×10^6 cells). The *in vivo* results demonstrate that ΔR_2^* mapping can be successfully used to quantify the cell population *in vivo*. The non-invasive nature of MR imaging makes such mapping very useful for drug delivery and tracking applications.

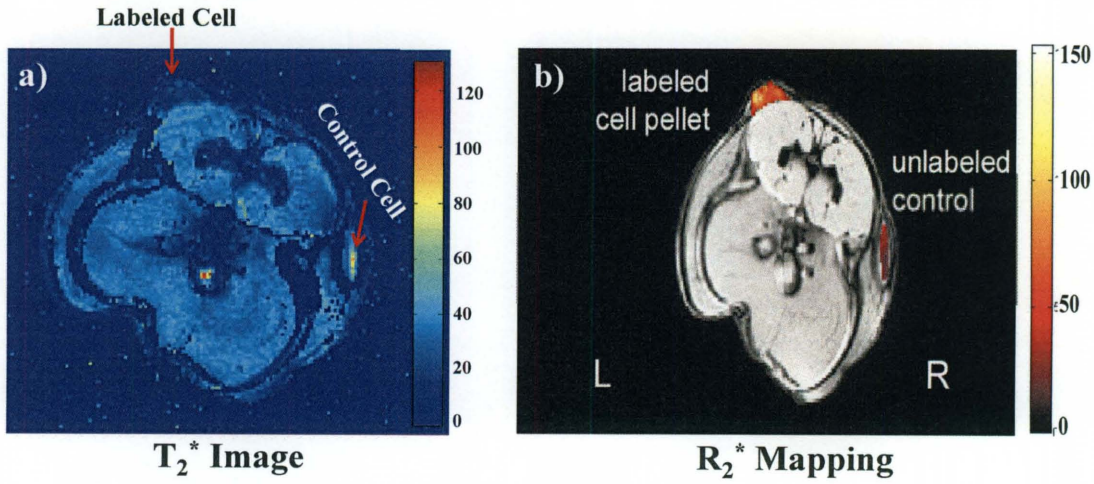

Figure 26. ***In vivo*** **relaxometry measurements of subcutaneously-injected cell pellets in a mouse at 3 T. (a) T2* map (in ms) of the injected cell pellets (b) R2* mapping (in s^{-1}) with two ROIs drawn for the cell pellets and overlaid onto an anatomical T2*-weighted image.**

Single-Cell Imaging

The ability to track a single cell or small population of cells will have a profound impact on our understanding of the disease and the diagnosis and treatment for them. For advanced biological applications such as stem cell therapy, tracking cancer cell metastasis requires the capacity to image a small population of cells.[30] Many different imaging modalities such as positron emission tomography (PET), optical imaging, and MRI are being actively investigated to achieve single-cell imaging.[59] MRI has fundamental advantages over other imaging modalities with deep tissue penetration, non-invasive nature, and good soft-tissue contrast. For cell tracking using MR imaging, the cells are usually labeled with CAs. The inherent low relaxivity (~ 4 $mM^{-1}s^{-1}$) of T_1-weighted paramagnetic CAs such as Gd-chelates and further loss of relaxivity upon cell internalization made them unsuitable for single cell imaging applications. However, T_2-weighted CAs (SPIOs) have recently been shown to provide sufficient contrast to track a single cell or small population of cells (<500 cells) both *in vitro* and *in vivo*. Single-cell imaging in MRI has been demonstrated using MPIOs and SPIOs.[60, 61] However, heavy labeling with CA was required to achieve single-cell visualization.[30] The strong R_2* effect of GNTs upon cell internalization allows single cells to be visualized *in vitro*. **Figure 27** shows the T_2* -weighted image of the sparsely-distributed *in vitro* cell phantom (5,500 cells/mL) at 9.4 T. **Figure 27a** shows the normal magnitude image of cells. **Figure 27b** shows the reconstruction using the susceptibility-weighted imaging (SWI) method, which reconstructs the image using the susceptibility differences in the sample. Dark spots were clearly seen in both of the images, but with the spots appearing much clearer in SWI reconstructed image. For GNT-labeled cells, the dark spots

originated from the presence of superparamagnetic GNTs. The GNTs induce a magnetic susceptibility effect in their local regions, generating field inhomogenity and thus extra dephasing around those regions. The susceptibility difference was utilized for the SWI reconstruction method. This is the first time single-cell visualization in MRI has been achieved using a non-iron oxide-based CA at 9.4 T (**Figure 27a and 27b**). SWI is a pure post-processing technique that requires no extra imaging time.

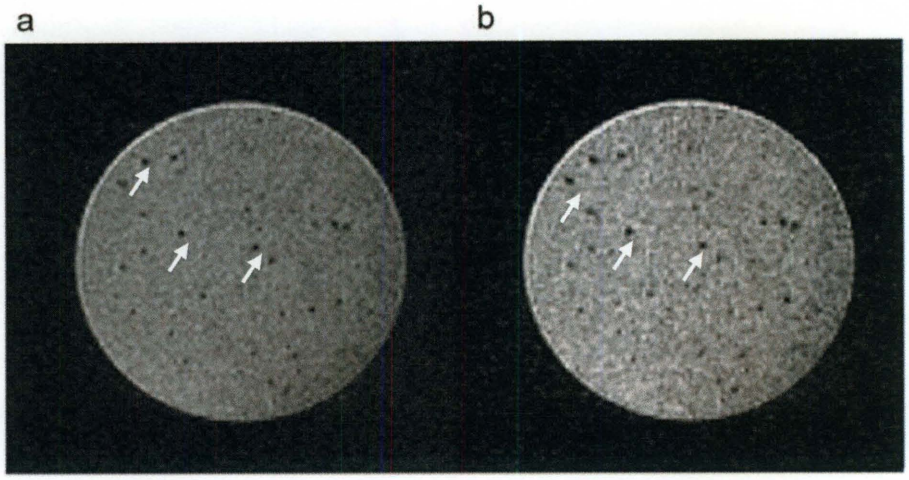

Figure 27. T_2*-weighted image of sparsely-distributed GNT-labeled J774 cells suspended in 1.0 % agarose gel at 9.4 T (a) Magnitude image and (b) susceptibility-weighted image (SWI).

The average intracellular uptake of GNTs in macrophages was determined to be 0.44±0.09 pg Gd^{3+}/cell using ICP-OES, corresponding to 1.69×10^9 Gd^{3+} ions/cell. This result is consistent with our previous study using serine-derivatized GNTs to label a MCF-7 human breast cancer cell line[57] and is two orders of magnitude greater (10^9 vs. 10^7 Gd^{3+} ions/cell) than when water-soluble gadofullerenes were used to label mesenchymal stem cells.[62] SPIOs have been shown to label macrophages at high loading levels via phagocytosis. However, for the high level of intracellular labeling needed to

achieve single-cell imaging, SPIO-based CAs require transfection agents. Our results show that macrophages can be labeled with lipophilic GNTs very efficiently (~20 pg/cell), without a transfection agent or advanced labeling techniques. The lipophilic nature of GNTs greatly facilitates their use for enhanced intracellular loading in different cell lines and allow for single-cell imaging.

CONCLUSION

GNTs exhibit exceptionally large and linear transverse relaxivities. When localized within the cell, the transverse relaxivities provide GNT with sufficient sensitivity for cellular imaging using MRI. The linear change in transverse relaxivities of GNTs can be used to track and quantify them *in vivo*. The large relaxivities also provide the ability to track a single cell or a small population of cells using GNTs as a labeling agent. The inherent lipophilic nature of the carbon nanotube materials makes them an attractive candidate to label cells efficiently without the aid of a transfection agent or advanced labeling techniques. However, to realize the complete potential of GNT materials for cellular and molecular imaging, studies focusing on the minimum threshold of the amount of GNTs per cell to detect them *in vivo* and the effect of aggregation on the transverse relaxivities of the GNTs need to be performed.

CHAPTER 5

Single-walled Carbon Nanotubes as T_2-weighted MRI CAs

Introduction

Nanomaterials with porous structures are attractive candidates for drug delivery applications. Drugs and molecules of biological interest can be confined within the pores in a chemically-inert atmosphere (nanoconstruct). The external surface of the nanoconstruct can be then chemically functionalized with targeting moieties to enable localized delivery of drugs. If carefully designed, such constructs can prevent premature release of drugs and undesired accumulation at non-targeted sites, which are the major drawbacks of current systemic delivery methods. Considering the advantages offered by such agents, a variety of nanomaterials such as gold nanoparticles,[63] silicon particles,[64] and SWNTs[65] have been studied for their potential for drug delivery applications.

Diagnostic imaging modalities can be used to track these agents *in vivo*. The imaging is achieved either by loading (or attaching) diagnostic agents in (or to) the nanoconstruct or by the inherent properties (magnetic, electronic or optical) of the nanoconstruct. For example, gold nanoparticles have near-infrared (NIR) absorbance,[66] silicon particles have been proposed as optical imaging agents,[67] and SWNTs have been shown to have vibrational signatures (Raman microscopy) and NIR fluorescence.[48, 49] In spite of having less tissue background fluorescence, NIR imaging still suffers from low tissue penetration. NIR imaging of SWNTs is dependent on the SWNT structure, and many of the functionalization techniques for SWNTs results in the disruption of the SWNT electronic structure, resulting in loss of NIR fluorescence. In the preceding

Chapter, the exceptionally high transverse relaxivities of GNTs and their ability to act as high-performance T_2-weighted MRI CAs was demonstrated both *in vitro* and *in vivo*. The high transverse relaxivities of GNTs enabled the first non-iron oxide-based single-cell imaging. The relaxation measurement studies revealed that US-tubes (with no Gd^{3+} ion) are excellent T_2-weighted MRI CAs. In fact, the majority of the transverse relaxation properties of the GNTs are expected to be from the US-tube component. It was hypothesized that the transverse relaxation properties (T_2-shortening) can be attributed to the presence of metal catalyst particles in US-tubes. In this Chapter, we characterized the magnetic properties of SWNT materials to understand the role of carbon SWNTs themselves on the transverse relaxation properties. In the previous Chapter, all of the studies were performed with SWNTs produced by arc-discharge process, which uses a binary metal catalyst (Ni, Y) in the synthesis. To circumvent the complications involved in understanding the magnetic properties of binary metal systems, SWNTs produced by high-pressure carbon monoxide method (HiPco) were used in this study. The HiPco-produced SWNTs have only a single metal catalyst (Fe) and still show T_2-shortening properties. In addition, HiPco SWNTs have a smaller diameter (~1.2 nm) compared to arc-produced SWNTs (1.4 nm), making HiPco SWNTs more reactive toward covalent functionalization than arc-produced SWNTs. Hence, for biological applications of SWNTs involving targeting using covalently-attached targeting moieties to the SWNT surface, HiPco SWNTs are preferred over arc-produced tubes.

MATERIALS AND METHODS

Synthesis of SWNT Materials

The raw SWNTs (r-SWNTs) produced by the HiP_{CO} process (Carbon Nanotechnologies, Inc) were used for this study. The HiPco SWNTs were grown with iron nanoparticles as catalyst. As obtained, r-SWNTs were then purified using a liquid bromine (Br_2) protocol developed in our laboratory.[68] This process not only removes the metal catalyst particle significantly (~ 6% remaining), but importantly does not disrupt the SWNT structure like many other acid purification processes. Most of the metal catlayst particles from outside the nanotube wall in r-SWNTs have been removed, and the remaining metal catalyst particles are mainly on the inside of the nanotube in purified SWNTs (p-SWNTs). Seperately, the r-SWNTs were cut into ultra-short SWNTs (US-tubes) by fluorination and pyrolysis in an inert atmosphere.[31] The cutting process produces nanocapsules with lengths predominantly between 20-80 nm. The fluorination also reduces the metal catalyst content further to a negligible level (0.6 % by weight) such that no catalyst particles are visible on the outside wall of US-tubes. However, it should be noted that the cutting process also produces significant damage to the nanotube sidewalls.

The iron content of each SWNT sample was determined using inductively-coupled plasma optical emission spectrometry (ICP-OES, Perkin-Elmer Optima 3200V). The measurements were run in triplicate and the average values were taken for concentration calculation. Magnetic properties of the samples were characterized with a Quantum Design MPMS-XL magnetometer based on a superconducting quantum interference device (SQUID) in the temperature range 5 – 300 K with an applied

magnetic field of 0.1 T. Samples were encapsulated in diamagnetic cellulose for measurements and run in duplicate. X-ray powder diffraction (XRD) data were obtained using a RigakuD/Max-2100PC diffractometer operating with unfiltered Copper Kα radiation (λ= 1.5406 Å) at 40 kV and 40 mA. The contribution from the Kα2 radiation was compensated for using the Rachinger algorithm. Goniometer alignment was verified by daily analysis of a Rigaku-supplied SiO_2 reference standard. Processing of the powder diffraction results and phase identification was accomplished using the program JADE.

In Vitro Relaxometry Measurements

The T_2-relaxation measurements were performed on a Bruker Minispec mq-60 (1.41 T) bench top relaxometer (Bruker Optics Inc, Billerica, MA) using Carr-Purcell-Meiboom-Gill (CPMG) sequence and phantom experiments were performed in a 3 T MRI system (General electric, Milwaukee, WI). The phantom images were obtained using 2D spin-echo imaging with a repetition time (TR) of 500 ms and echo times (TEs) ranging from 10 to 50 ms in either 5 or 10 ms increments.

The three SWNT materials (r-SWNTs, p-SWNTs, and US-tubes) studied were dispersed in equal volumes of bio-compatible Pluronic® (polyethylene oxide-polypropylene oxide block co-polymer) surfactant using probe sonication for the MRI studies. The sonicated solutions were allowed to settle overnight and centrifuged (3200 rpm for 15 minutes) to produce mostly individual tubes or very small bundles in solution. The supernatant was collected and dialyzed (50,000 MW cutoff membrane) to remove any excess surfactant.

The T_2-relaxation time (ms) per mg of the SWNT sample (**Table XIII**) was calculated using the linear relationship between the concentration and relaxation time (i.e. as the concentration increases the relaxation time (T_2) decreases). Based on the iron

content, the respective amount of SWNT material present was calculated for the given volume used for the relaxation time measurement. Finally, the T_2-relaxation time was normalized for one mg of the SWNT material.

RESULTS AND DISCUSSION

The effect of SWNT materials on T_2 relaxation times have been previously reported, however, such observation has been reported for only r-SWNTs (> 1 μm in length) and the T_2 relaxation properties of the SWNT materials was attributed to the metal catalyst impurities (Fe for HiPco-produced SWNTs) present.[52, 69] Metal mediated toxicity is a major concern for carbon nanotube based biomedical applications.[70] The metal catalyst particles cover the tube ends of r-SWNTs,[52] which might prevent loading of biologically interesting molecules into the interior of the SWNTs. In addition, the exact length of SWNTs suitable for biological applications is not known, however, SWNTs with length < 300 nm has been shown to be renally excreted, and renal excretion is an important consideration for any nanoparticle-based biological applications.[71]

In order to better understand the role of the metal catalyst particles and the length of SWNTs on MRI relaxation properties, r-SWNTs, p-SWNTs, and US-tubes were compared. We chose to purify the tubes using liquid Br_2 method than commonly-known acid purification processes to preserve the electronic and physical structure of r-SWNTs. US-tubes, in addition to being shorter in length, also provide more available surface-to-volume ratio (**Table X**), which might be advantageous for drug delivery applications. In our laboratory, we have previously loaded the US-tubes with magnetic materials for MR imaging,[18] molecular iodine for X-ray CT imaging,[16]

and α-emitting agents (^{211}At) for radiotherapy of cancer.[17]

Table X. Surface area measurements of SWNT materials

	p-SWNTs	US-tubes
BET surface area (m^2/g)	574 (0.999056)	980 (0.998694)
Langmuir surface area (m^2/g)	870 (0.998647)	1478 (0.999072)

Transverse Relaxivities of SWNT Materials

The spin-lattice relaxation time (T_2) of all the three SWNT materials is presented in **Table XI**. The T_2 values are dependent on the concentration of the materials. Hence, in order to compare the effect of the SWNT materials, it is necessary to compare their relaxivity which is normalized for concentration. Calculating the concentration of nanotubes (mM) in solution is very difficult considering the vast differences in length and the presence of metal catalyst particles. An alternate way of identifying the actual role of nanotubes on the MRI relaxation properties is to identify the relaxation properties of the metal catalyst particles and assign the rest of the effect to the nanotubes. The presence of single metal catalyst particles in HiPco tubes is helpful for such characterizations. In addition, the iron particles have been extensively studied for their MRI relaxation properties and are well-documented.[47]

The relaxivity of the three types of SWNTs to act as T_2-weighted MRI CAs based on their metal catalyst (Fe) concentration is presented in **Table X1**. All three SWNTs showed remarkably short T_2 relaxation times. But by comparing the relaxivities (r_2) of the samples, which are normalized for the metal catalyst

concentration, it has been determined that a higher concentration of metal catalyst nanoparticles does not necessarily mean better T_2-relaxation properties, since, p-SWNTs are about as effective a T_2-shortening agent as r-SWNTs in spite of having three times less iron. Despite having ~28 times less iron, the US-tubes are only marginally inferior (~ 2 times) to r-SWNTs in shortening T_2. Comparison of the relaxivity, which is normalized for concentration, shows that p-SWNTs and US-tubes are much superior to r-SWNTs. This observation is contrary to the reported role of metal catalyst particles on the relaxation properties of SWNTs.[52, 69] Furthermore, the US-tubes, which have the smallest iron content by far, possess the highest relaxivity.

Table XI. Relaxation times of aqueous SWNT suspension. Measurements were performed at 60 MHz & 37 °C. For comparison, a clinically-used SPIO T_2-agent (Ferumoxtran®) is also included. [Ref 30] *Based on iron concentration.

Sample	[Fe] mM	T_1 (ms)	T_2 (ms)	r_1 ($mM^{-1}s^{-1}$)*	r_2 ($mM^{-1}s^{-1}$)*	r_2/r_1
r-SWNT	0.449	-	34.6	-	63.6	-
p-SWNT	0.167	242.2	46.5	22.8	126.8	5.6
US-tube	0.075	1000	67.7	8.9	192.5	21.6
Ferumoxtran-10	-	-	-	9.9	65	6.6

To be effective as CAs for advanced applications such as molecular and cellular imaging, T_2-shortening CAs are expected to have a more pronounced effect on the spin-spin (T_2) relaxation time than on the spin-lattice (T_1) relaxation time (greater r_2/r_1 ratio). For example, Ferumoxtran®, widely and successfully used as a T_2-weighted MRI CA, exhibits an r_2/r_1 ratio of ~ 6 (Table 10). Both p-SWNTs (r_2/r_1 >5) and US-tubes (r_2/r_1 >20) are very effective as T_2-weighted CAs, but the US-tubes are superior to the clinically-used agent and possibly more suitable for specialized applications such as imaging

biological processes at the molecular level. In fact, their superior r_2 efficiency and exceptionally large r_2/r_1 ratio, along with their shorter length (< 100 nm), makes the US-tubes unique candidates for such applications.

The relaxivity measurements mentioned above are the accepted standard by which CAs are compared. However, to test their efficiency in a clinical setting, the SWNT-based CAs were tested for their efficacy in a 3 T clinical scanner. The three SWNT materials exhibit different degrees of dispersion in Pluronic® surfactant. Homogenous sample concentration is preferred for the phantom experiments, so, dilutions were made to produce an equal amount of the SWNTs in all three samples. In order to make homogenous solutions, known quantities of each of the three materials in the absence of surfactant were analyzed for their iron content by ICP-OES. The ICP measurements were run in triplicates (agreement within 2%) to determine the average iron content in each sample, as shown in **Table XI**. Then the SWNT samples dispersed in Pluronic® surfactant were analyzed for their iron content, and, from these values, the amount of SWNTs present in each of the sample was determined. The samples were then diluted such that the concentration of SWNTs in each sample was the same (360 ± 4 mg of SWNTs/L) as shown in **Table XII**. The phantom image of the samples (**Figure 28**) represents the loss of signal as a function of different echo times (TE). The faster the loss of signal, the shorter is the T_2-relaxation time. As can be seen in the image, both r-SWNTs and p-SWNTs have much shorter T_2-relaxation times than US-tubes. The actual values of the T_2-relaxation time of all the three SWNT samples are presented in **Table XII**. Their relaxivity, normalized for their metal catalyst concentration, is also presented in **Table XII**. As observed with the bench-top relaxometer, both p-SWNTs and US-tubes

are much superior relaxation agents to r-SWNTs. The observed differences in the relaxivity between the 1.5 T bench-top scanner (**Table XI**) and the 3 T (**Table XII**) clinical scanner is likely due to the dependence of T_2 on magnetic field strength and the better optimized imaging parameters in the clinical scanner.

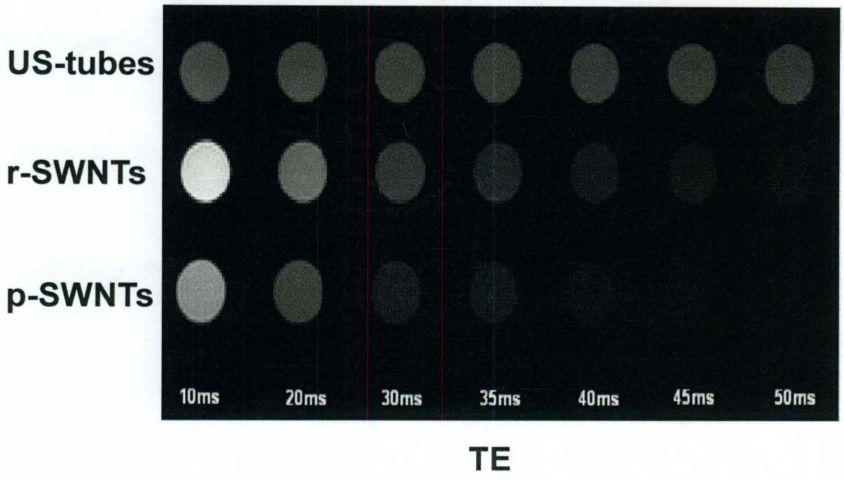

Figure 28. T_2-weighted MRI phantom images of the aqueous SWNT solutions in a 3 T scanner.

Table XII. Transverse relaxivities (r_2) of aqueous SWNT suspension. Data collected in a 3 T scanner at 37 °C. All samples are at a concentration of 360 ± 4 mg SWNTs/L. * Based on iron concentration.

Sample	Fe % (%wt)	Fe concentration (mM)	T_2 (ms)	r_2 relaxivity ($mM^{-1}s^{-1}$)*
r- SWNTs	17.2 ± 0.2	1.11	13.6	65
p-SWNTs	6.1 ± 0.2	0.40	15.1	166
US-tubes	0.63 ± 0.15	0.04	94.1	230

X-Ray Diffraction Studies of SWNT Materials

The superior contrast enhancement properties of the SWNT materials and the observed difference in the relaxation efficiency among the three SWNTs samples studied cannot be assigned to the SWNT structure, unless the nature of metal catalyst particles is compared between SWNT samples. The comparison of the chemical nature of the metal catalyst particles present in each of the SWNT materials is necessitated by the chemical processes involved in the preparation of p-SWNTs and US-tubes such as purification by Br_2 and acid washing using concentrated HCl. X-ray diffraction (XRD) studies were performed on all three SWNT samples. The US-tubes did not show any observable XRD peaks, which undoubtedly is due to their low iron content (< 1%). XRD data for the r-SWNT and p-SWNT samples are given in **Figure 29**. As shown in the figure, both samples display similar XRD patterns. The peaks shown were assigned using JADE software, and the best fit was observed for Fe_3O_4. The XRD results demonstrate that the r-SWNT and p-SWNT materials are similar with respect to the iron particles present and that these iron particles are predominantly Fe_3O_4.

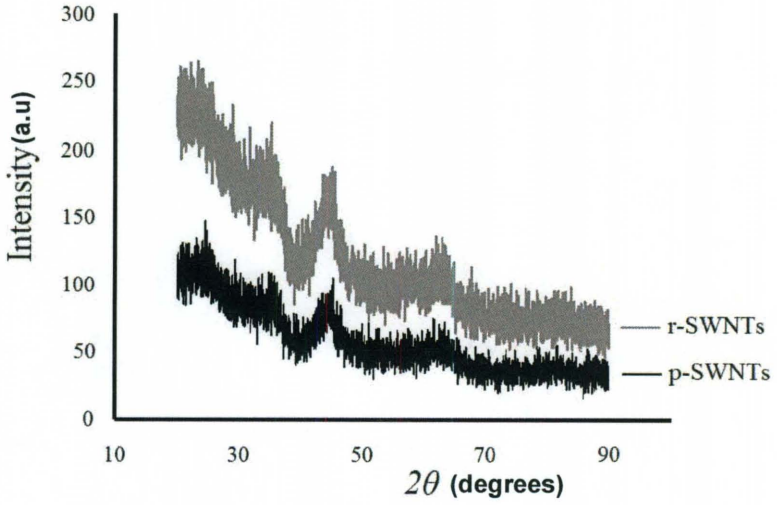

Figure 29. Powder X-ray Diffraction pattern of the SWNT materials.

Magnetic Characterization of SWNT Materials

The absence of XRD peaks for US-tubes makes it difficult to understand the chemical nature of metal catalyst particles in US-tubes. However, the XRD patterns of p-SWNTs and r-SWNTs suggest that the chemical nature of the metal catalyst particles cannot be the reason for the observed difference in relaxivity. The ability of any material to act as an MRI CA is determined mainly by their magnetic properties. Fe_3O_4 particles can act either as a ferromagnetic or superparamagnetic material depending on particle size.[72, 73] In addition, most of the chemical processes involved in the synthesis of p-SWNTs and US-tubes from r-SWNTs are standardized procedures aimed at developing nanotube materials suitable for biological applications. Hence, magnetic characterization of the SWNT materials as such (without modifying the processes) would be more informative and reproducible for real time applications. The SWNT materials were characterized for their magnetic properties by SQUID magnetometry (**Figure 30**). The r-SWNTs (**Figure 30a**), p-SWNTs (**Figure 30b**), and US-tubes (**Figure 30c**) data are all consistent with superparamagnetism: the zero-field-cooled (ZFC) curves are characterized by a *mean* blocking temperature, T_B, above which the material is superparamagnetic and below which magnetic viscosity gives rise to a hysteretic magnetization loop. This arc nature of the zero-field-cooled (ZFC) or field-cooled (FC) curve is representative of either superparamagnetism or spin-glass state. However, the FC curve in all the SWNTs samples are reversible, ruling out the possibility of the presence of spin-glass system.[74] Furthermore, the maximum blocking temperature, $T_{B,max}$, or the temperature where initial bifurcation between the ZFC and FC curves occurs, decreases with purification from r-SWNTs to US-tubes (**Figure 30**). This indicates that as $T_{B,max}$

approaches T_B, the net distribution of superparamagnetic domain sizes become more uniform. The magnetic characterization of the SWNT materials also provides information about the average size of the metal catalyst particles assuming the observed magnetic properties are that of metal catalyst particles. Using a T_B of 40 K and the magnetic anisotropy constant K of bulk Fe_3O_4, 4 x 10^5 erg cm^{-3} (the majority of residual catalyst in HiP_{CO} SWNTs exists as magnetite),[75] we calculate a mean particle volume V = 3.45 x 10^{-19} cm^3, or a mean particle radius r = 4.35 nm using $T_B = KV / 25k_B$,[76] and slightly smaller particles for US-tubes. When compared to similarly-sized iron oxide particles (2-4 nm) with r_2 = 72 $mM^{-1}s^{-1}$, the p-SWNTs and US-tubes far outperform their solely iron oxide-based counterpart.[77]

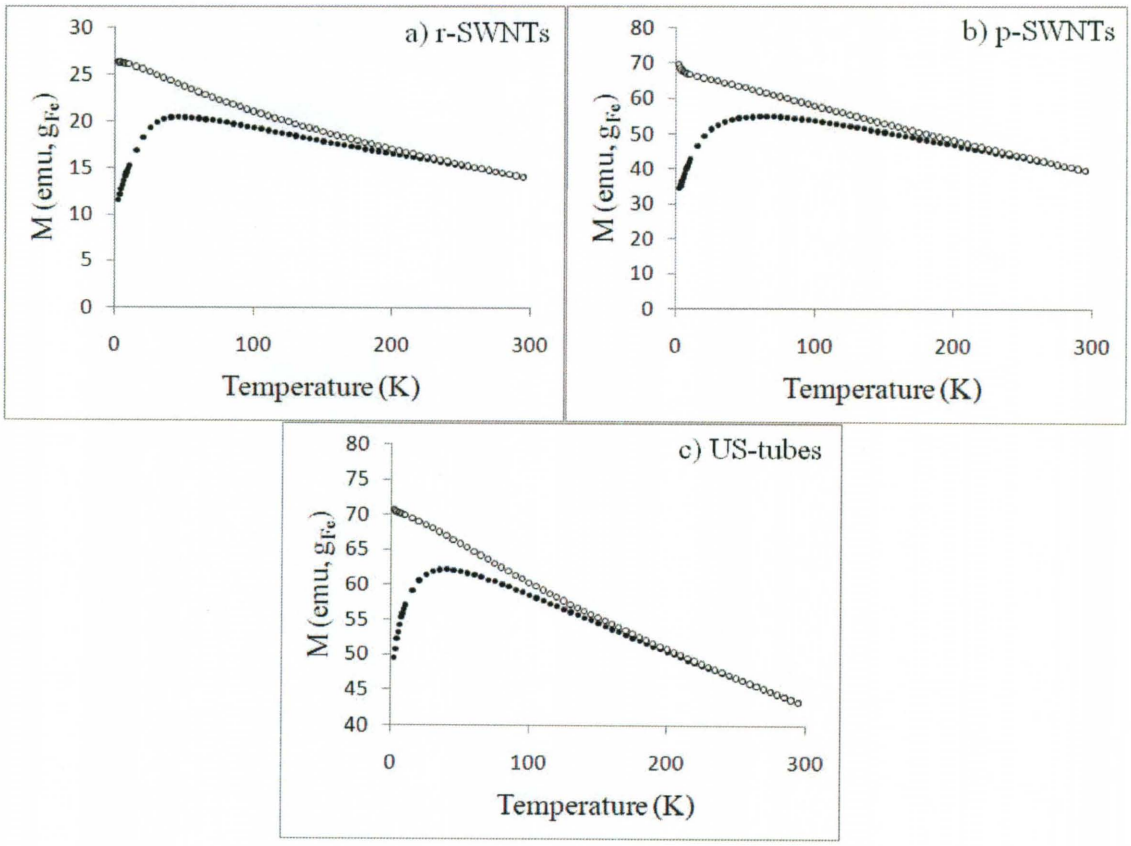

Figure 30. Zero-field-cooled [black] and field-cooled [gray] magnetization curves for a) r-SWNTs b) p-SWNTs c) US-tubes. Applied magnetic field is 0.1 T.

Role of SWNTs on Transverse Relaxivities of SWNT Materials

Complete characterization of the metal catalyst nanoparticles in US-tubes by XRD is not available. However, the magnetic measurements reveal that the US-tubes are not significantly different from r-SWNTs and p-SWNTs in their magnetic properties. Hence, the superior relaxivity of the SWNT materials, and especially of the US-tubes and p-SWNTs, clearly suggests that the role of the carbon SWNTs themselves should not be ignored when interpreting the resultant magnetic and T_2-relaxation properties. There are few reports on the literature documenting inherent magnetic properties of SWNTs.[78, 79] In fact, finite zigzag carbon nanotube materials are shown to be inherently paramagnetic. The magnetic properties are attributed to their chirality, diameter, and length, with shorter-length tubes being potentially more magnetic.[78] In case of US-tubes, the abundance of defect sites on the SWNT surface could also add to the magnetic properties in the nanotube materials as well.[79] These results all suggest that it is not correct to assign the magnetic properties of SWNT materials to metal catalyst nanoparticles alone. In fact, superparamagnetic SWNT materials may be a distinct new class of T_2-weighted MRI CA with performance contributions from both iron oxide and the carbon SWNT material itself. Hence, their T_2-relaxation times are probably better expressed as a function of SWNT material concentration ($ms.mg^{-1}$), as also presented in **Table XIII**. Calculating the exact contribution of SWNT materials has not been achieved due to the non-availability of SWNT materials completely devoid of metal catalyst nanoparticles.

Table XIII. T_2-relaxation times of SWNT samples per mg of SWNT materials.

Sample	r-SWNT	p-SWNT	US-tube
T_2 (ms/mg)	4.6	5.1	31.7

CONCLUSION

The synergistic effect of metal catalyst nanoparticles and carbon SWNTs offer a new paradigm in T_2-weighted MR imaging. The lipophilic nature of SWNTs provides them the ability to translocate the cell membrane without the help of any transfection agents. The bioinert nature of the SWNTs and the recent advancements in their functionalization chemistry makes them appealing for cell and gene delivery applications. Our results suggest that the magnetic properties of SWNTs, even in the presence of negligible amount (< 1%) of metal catalyst particles, offer a way to track them *in vivo* using MRI. The superior relaxivity of the p-SWNTs and US-tubes over the r-SWNTs is also noteworthy since these materials, when used as *in vivo* MRI agents, should demonstrate better sample purity and reduced metal-mediated toxicity. US-tubes, with their shorter length, superior relaxivity, and negligible metal content appear to be the most promising SWNT material of all for *in vivo* magnetic cell labeling/trafficking studies and other molecular imaging applications.

CHAPTER 6

Optimizing the Contrast Enhancement of Gd-Based CAs by Geometrical Confinement

Need For Optimization

The design and synthesis of new clinical MRI CAs has seen enormous progress in recent years. Generally, most of the clinically used CAs have relaxivities smaller than 4 $mM^{-1}s^{-1}$ (**Table XIII**). Theoretical models predicts the possibility of much larger relaxivities for Gd-chelates ($\geq$ 150 $mM^{-1}s^{-1}$ per Gd^{3+} ion) with optimized electronic, exchange, and motional correlation properties.[9] Hence, there is a constant effort to design new MRI CA systems with optimized properties. In this work, we demonstrate the use of geometrical confinement to enhance the longitudinal relaxivity (r_1) of Gd-based CAs. Intravascularly-injectable nanoporous silicon particles (SiMPs) were used as the confinement platform and individual GNTs as the Gd-based CA.

Table XIV. Longitudinal relaxivities of clinically-used Gd-chelates at 1.41 T and 37 °C.

CA	r_1 [$mM^{-1}s^{-1}$] per Gd^{3+} ion
Gd-DTPA [10]	3.4
Gd-DOTA [10]	3.1
Gd-DTPA-BMA [10]	3.6
Gd-HP-DO3A [10]	3.2
Gd-HP-DO3A [10]	3.2
Gd-BOPTA [10]	4.1

MATERIALS AND METHODS

Fabrication, surface modification and characterization of mesoporous Si particles (SiMPs)

Hemispherical porous silicon particles with 1.6 μm diameter and discoidal porous silicon particles with 1.0 μm diameter and 400 nm thickness were used in the study. All the particles were fabricated in the Microelectronics Research Center at The University of Texas at Austin by combination of standard photolithography and electrochemical etching. Hemispherical particles were fabricated following protocols previously reported.[64] Discoidal particles were fabricated by newly developed protocols: briefly, heavily doped p++ type (100) silicon wafers with resistivity of 0.005 ohm-cm (Silicon Quest, Inc, Santa Clara, CA) were used as the silicon source. A 400 nm porosity layer was formed by applying a 7 mA/cm current for 125" in a 1:3 HF (49 %) ethanol solution. The electrical current was then increased to 76 mA/cm and applied for 8" forming a high porosity release layer. A 40 nm SiO_2 layer was deposited by low pressure chemical vapor deposition at 400 °C. Standard photolithography was used to pattern a 1.0 μm circular pattern with 1.0 μm pitch over the SiO_2 capped porous layer using a contact aligner (K.Suss MA6 mask aligner) and NR9-500P photoresist (Futurrex Franklin, NJ, USA). The pattern was transferred into the porous double layer by dry etching in CF_4 plasma (Plasmatherm 790, 25sccm CF_4, 100 mTorr, 200W RF). The capping SiO_2 layer was removed in 49 % HF, and the particles were released from the substrate by sonication in isopropanol. The particles were treated with H_2O_2 at 100 °C to oxidize the surface.

Fabrication and surface modification of GNTs

Individual GNTs were synthesized using the protocol described in detail in Chapter 2, Materials and Methods section.

Fabrication and surface modification of GFs

Polyhydroxylated Gadofullerenes [$Gd@C_{60}(OH)_x$; x ~27] (obtained from TDA Research Inc.) were dissolved in HPLC grade water. The resulting solution was passed through a 0.2 μm filter and centrifuged at 3200 rpm for 10 minutes. The resulting supernatant solution was used for loading and MRI characterization.

Loading of the porous Si particles (SiMPs) with Magnevist® (MAG), Gadofullerenes (GFs), and Gadonanotubes (GNTs)

For loading the pores of the Si particles with the Gd-CAs, known amounts of mesoporous silicon particles were lyophilized to dryness for 6 hours in non-stick plastic tubes using Labconco® FreeZone™ Freeze Dryer system. Two protocols were tested: (1) single-step loading and (2) sequential loading. During the first experimental setup, dry Si particles were mixed with 300 μL of Gd-CAs (Magnevist, GNTs or GFs) solution. The resulting suspension was sonicated (30 W bath sonicator) for 5 minutes and centrifuged for 10 min at 3200 rpm. The supernatant was discarded and the flocculated particles were washed twice with DI water to remove any excess of Gd-CAs adhering to the outer surface of the Si particles. For the sequential loading experiments, the Si particles were introduced initially into 100 μL of Gd-CAs stock solutions, followed by sonication and centrifugation. After the supernatant was discarded, another 100 μL of the stock solution was added, followed by sonication and centrifugation. The process was repeated with

addition of another 100 µL of stock solution (total volume of the stock solution added is 300 µlL), followed by loading and washing twice with DI water. In order to estimate the efficiency of loading, the particles were dissolved in 1 N NaOH overnight. The resulting solution was treated with ~26 % $HClO_3$ and heated to dryness. The resulting precipitate was dissolved in 2 % HNO_3 and Gd^{3+} ions released from the particles during the degradation process were analyzed using ICP-OES.

Scanning electron microscopy

Samples were mounted on SEM stubs (Ted Pella, Inc.) either using conductive adhesive tape (12 mm OD PELCO Tabs, Ted Pella, Inc.) or by applying wet samples to stubs and air drying in a desiccator. Samples were sputter coated with a 10 nm layer of gold using a Plasma Sciences CrC-150 Sputtering System (Torr International, Inc.). SEM images were acquired under high vacuum, at 20.00-30.00 kV, spot size 3.5-5.0, using a FEI Quanta 400 FEG ESEM equipped with an ETD (SE) detector.

Relaxometry studies

T_1-relaxation times of GNTs in nanoporous silicon particles were measured in a Bruker Minispec bench-top relaxometer operating at 60 MHz and 37 °C. T_1-relaxation times were measured using inversion recovery sequence and HPLC grade water was used as diamagnetic control.

Phantom studies in clinical scanner were performed in a 1.5 T commercial scanner (Achieva, Philips Medical Systems, Best, The Netherlands) equipped with a 32-channel radiofrequency system. A 32- or 16-element phased-array surface coil was used

for MR signal reception. An inversion recovery sequence was used for image acquisition with TR = 7500 ms and TE = 20 ms.

RESULTS AND DISCUSSION

The SiMPs were microfabricated using a combination of photolithography and electrochemical etching that allows for controlling the size, shape, and porosity of the particles.[64, 80] The shape can be hemispherical, quasi-hemispherical, or discoidal with an effective diameter ranging from 600 nm to a few microns. The diameter of the pores can be tailored to be between 10 nm (small pores) and 100 nm (large pores). GNTs were loaded within the nanopores of quasi-hemispherical (H-SiMPs) particles, with a nominal diameter of 1.6 μm and thickness of about 1 μm, and discoidal (D-SiMPs) particles, with a nominal diameter of 1.0 μm and thickness of about 0.4 μm (**Figure 31**). The average pore size ranges between 30-40 nm for both SiMPs.

The generality of our procedure was also tested for two other Gd-based CAs, namely Magnevist® (MAG), and gadofullerols (GFs). Magnevist (Gd-DTPA) is a gadolinium polyaminocarboxylate complex (**Figure 31a**), widely used in the clinic as a T_1-weighted MRI CA.[10] GFs are new carbon nanostructure-based lipophilic CAs showing enormous promise as MRI CAs.[81] GFs used in this study have a single Gd^{3+} ion encapsulated by a spherical C_{60} fullerene cage of ~ 0.7 nm in diameter (**Figure 31b**). The external fullerene cage prevents the leaking of the Gd^{+3} ions, and a functionalization platform for solubility and biocompatibility. It is important to note that GFs are known to aggregate in solution even after functionalization.

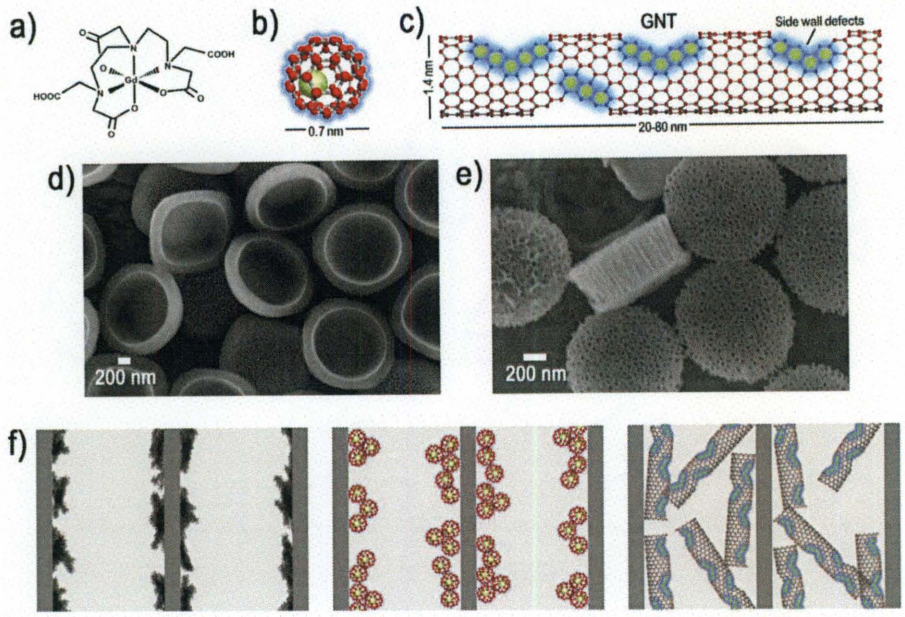

Figure 31. Schematic representation of the Gd-based CAs: a) Magnevist®, b) a GF, and c) a individual GNT. d) & e) SEM images of hemispherical and discoidal Si particles, respectively. f) schematic representation of the confinement of the Gd-CAs in nanoporous SiMPs.

Comparison of Loading Protocols

The loading and confinement of GNTs within the SiMPs occurs primarily through capillary forces.[82] Two different loading procedures were attempted in this study: i) a single-step loading and ii) a sequential loading. In the sequential loading process, a concentrated solution of GNTs ($[Gd^{3+}]$ = ~67 μM) was exposed to SiMPs in a stepwise fashion. The SiMPs were washed with HPLC grade water after each step. The amount of Gd^{3+} ions loaded within the nanoconstructs was determined by ICP-OES. The two loading procedures showed no difference in the concentration of Gd^{3+} ions confined within SiMPs (**Figure 32**). Some GNTs were seen adhering to the outer surface of SiMPs in the single step loading procedure (**Figure 33 A**). In contrast, sequentially-loaded

SiMPs showed no such external adhesion, suggesting complete entrapment of GNTs in the nanopores (**Figure 33 B**). Hence, the sequential loading process was used for the preparation, characterization, and study of the nanoconstructs. A similar sequential loading protocol was also used for loading and confinement of MAG and GFs within SiMPs.

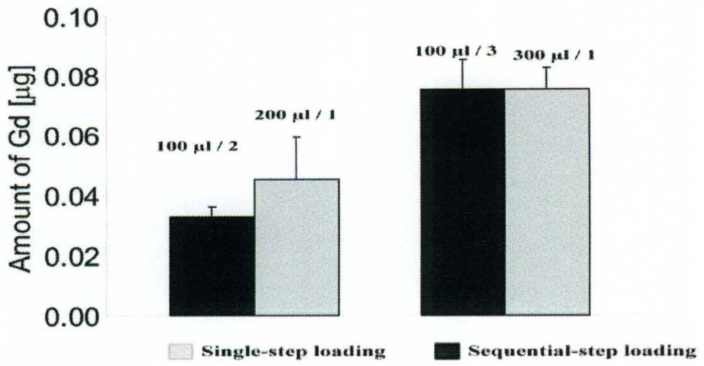

Figure 32. Comparison of the two loading protocols used for the geometrical confinement of GNTs in SiMPs.

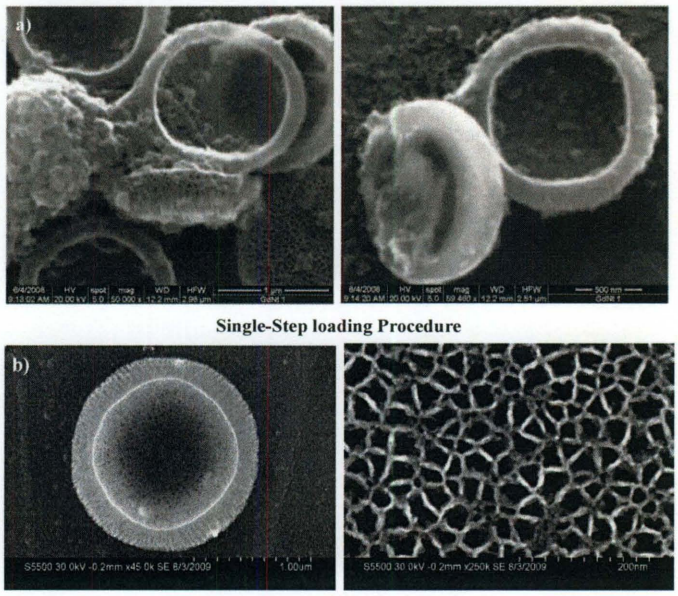

Figure 33. SEM images of a) SiMPs loaded with GNTs using the single-step procedure or b) SiMPs loaded with GNTs using the sequential loading procedure.

Magnetic Characterization of Gd-CAs/SiMP Nanoconstruct

A bench-top relaxometer (Bruker Minispec mq-60; 60 MHz) was used for the T_1-relaxation measurements of our nanoconstructs. Empty SiMPs alone showed no observable relaxation properties. **Figure 34** represents the longitudinal relaxivities (r_1) measured for six different nanoconstructs using a bench-top relaxometer. Compared to the Gd-CAs (GNTs, GFs, MAG) alone, the nanoconstructs exhibited significantly higher r_1. To test the ability of the CA in clinical settings, we performed phantom measurements on representative H-SiMP/GNT nanoconstruct in a clinical 1.5 T scanner (**Figure 35**). The H-SiMP/GNT construct showed a significantly lower inversion time (T_{inv}= ~1200 ms) compared to empty SiMP (T_{inv}= ~1700 ms), demonstrating that the contrast enhancement is due to the GNTs within the H-SiMP/GNT nanoconstruct.

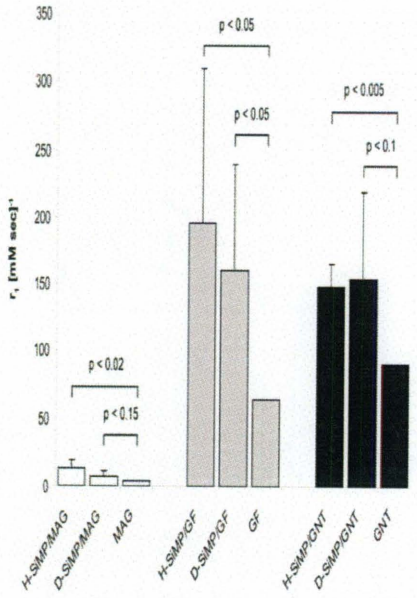

Nanoconstruct	r_1 [mM^{-1}sec^{-1}]	Ratio
H-SiMP/MAG	13.31 ± 6.13	3.33
D-SiMP/MAG	6.63 ± 4.34	1.66
MAG	4	-
H-SiMP/GF	195.39 ± 114.51	3.05
D-SiMP/GF	151.98 ± 59.74	2.50
GF	64.10	-
H-SiMP/GNT	147.90 ± 17.21	1.64
D-SiMP/GNT	150.72 ± 68.90	1.67
GNT	90.00	-

Figure 34. Longitudinal relaxivities of the six different Gd-CA/SiMP nanoconstructs.

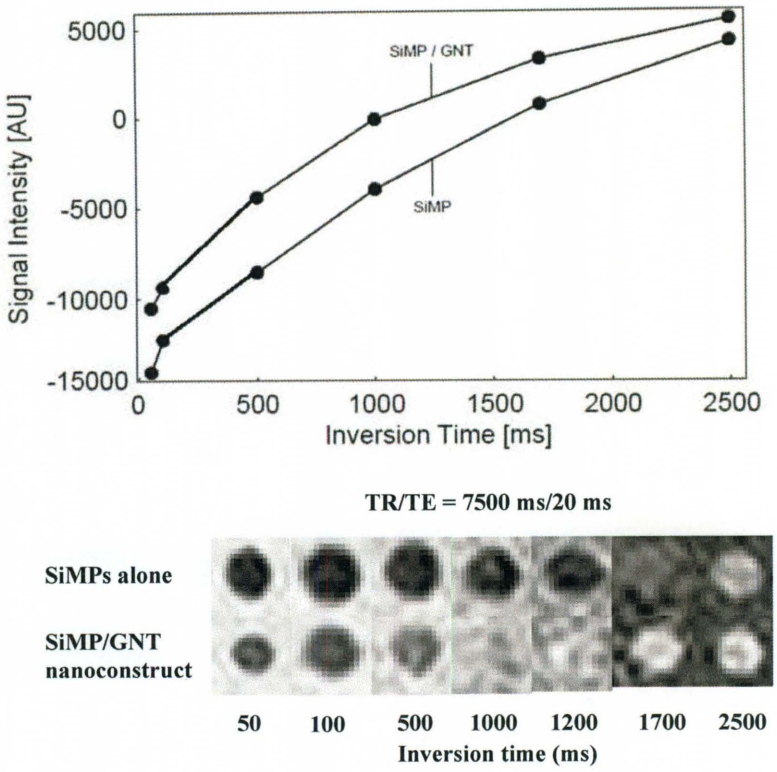

Figure 35. Phantom measurements in a clinical 1.5 T MRI scanner.

Rationale behind Improved Relaxivity

The longitudinal relaxivity (r_1) of a CA has two components: the inner-sphere relaxivity r_1^{IS}, and the outer-sphere relaxivity r_1^{OS}. The outer-sphere mechanism involves random translation diffusion of bulk water in the vicinity of paramagnetic center and as a result can be hardly modified. Hence, most of the research about the design of new, high-efficiency CAs focuses on optimizing the inner-sphere parameters to optimize the relaxivity. Inner-sphere parameters include the number of inner-sphere water molecules (q), the molecular tumbling time of the CA with inner-sphere water molecules (τ_R), and the proton residence time (τ_m) of the water molecules in the inner-sphere.

This has lead to the development of a number of nanoparticle-based CA constructs. Paramagnetic liposomes containing Gd^{3+}-ions (r_1=11 $mM^{-1}s^{-1}$ at 25 MHz),[83] a dendrimer-based nanoprobe, obtained by covalent attachment of Gd-chelates to PAMAM dendrimers (r_1=20 $mM^{-1}s^{-1}$ at 130 MHz),[84] Gd^{3+}-complexes bound to human serum albumin (r_1 = 130 $mM^{-1}s^{-1}$ at 20 MHz),[85]and chelation of Gd^{3+} ions with protein molecules (r_1= 130 $mM^{-1}s^{-1}$ at 65 MHz)[86] have all been shown to be effective at improving relaxivity. Most of these studies are based on engineering the bond between Gd^{3+} ions and surrounding molecules, with the aim of increasing the rate of water exchange (reduced τ_m) and the characteristic tumbling time (τ_R), and thus, require a specific interaction. However, our method is a more general approach for enhancing the longitudinal relaxivity (r_1) of Gd-CAs, namely, that the characteristic parameters q, τ_R, τ_m, and τ_D can be appropriately modified by confining the CA within a nanoporous matrix.

The role of geometrical confinement on the above-mentioned parameters of the nanoconstructs was analyzed to interpret the observed boost in their relaxivity. The bench-top relaxometer results and clinical phantom studies confirmed that the SiMPs themselves do not have any proton relaxation properties. For Magnevist®, the inner-sphere and outer-sphere mechanism contribute nearly equally to the longitudinal relaxivity. The effect of confining MAG within the pores SiMPs can be several-fold: increase the molecular tumbling time τ_R (inner-sphere), reduce the mobility of the outer-sphere water molecules, thus increasing the diffusion correlation time, τ_D (outer-sphere), and alter the proton residence time (τ_m) of inner-sphere water molecules inside the pores.

The GFs/SiMP nanoconstructs exhibited large standard deviations in relaxivity. The observed relaxivity variations are most likely due to presence of empty fullerenes (nearly 60 %) in the GF stock solution. The inability to separate $Gd@C_{60}$ fullerenes completely from empty C_{60} fullerenes is, in fact, a concern for metallofullerene-based biological applications. The interpretation of the improved relaxivity of GFs/SiMP nanoconstruct is even more challenging because of the unique and still not fully understood behavior of GF themselves.[46] The presence of hydrophobic C_{60} fullerene cage prevents any direct interaction between Gd^{3+} ion center and water protons. Such shielding suggests no traditional inner-sphere like mechanism is possible for GFs. However, the hydroxyl groups (in $Gd@C_{60}(OH)_x$) on the surface of the fullerene cage leads to an inner-sphere like mechanism. GFs exist as aggregates even after functionalization. Initial studies attributed the aggregation leading to a lower tumbling time (τ_R) as the reason for the improved relaxivity of GFs.[87] However, it was recently reported that the water molecules trapped in the interstices of these aggregates (larger diffusion correlation times τ_D) are likely the source for improved relaxivity of GFs.[46] The loading of GFs into nanopores could favor aggregation and possibly coordinate interactions among adjacent clusters of GFs. Confining GFs within the nanoconstruct might also lead to an increase in diffusion correlation time (τ_D). However, a thorough interpretation of the enhancement in relaxivity due to geometrical confinement of GFs is only possible with nanoconstruct loaded with only GFs and not empty fullerenes as well.

GNTs are much more homogenous than GFs. The parameters likely affecting the relaxivity of individual GNTs are already predicted using the SBM theory (**Chapter 3; Table III**). The slow molecular tumbling (greater τ_R) of GNTs suggests that inner-sphere

relaxivity is the most dominant mechanism of GNTs.[45] The nanoconstruct obtained by loading individual GNTs into the SiMPs (quasi-hemispherical and discoidal) demonstrated a r_1 relaxivity of ~150 $mM^{-1}s^{-1}$ at 1.41T, which is significantly larger than the ~90 $mM^{-1}s^{-1}$ observed for the individual GNTs before loading. The increase in relaxivity observed for the nanoconstruct is likely due to the organization of individual GNTs within the pores. Inside the pores, GNTs packed in close proximity to one another resemble a uniform GNT aggregate (pseudo-aggregation). The pseudo-aggregation of GNTs within the nanopores is further corroborated by the relaxivity of GNT/SiMP nanoconstruct (~ 150 $mM^{-1}s^{-1}$ per Gd^{3+} ion) which resembles that of bundled GNTs (~ 170 $mM^{-1}s^{-1}$). Pseudo-aggregation of GNTs inside SiMPs could result in water molecules getting trapped in the interstices of the GNT aggregates. Water molecules trapped between GNTs inside SiMPs could enhance the overall relaxivity of the nanoconstruct like second sphere water molecules in the case of some more common Gd-complexes.[88] In addition, the confinement of GNTs within the SiMPs could increase their tumbling time, τ_R, to an even greater extent because of the contact with the pore walls and an increase in effective viscosity of the water molecules trapped within the pores.

CONCLUSION

In summary, we show that confinement of MRI CAs in nanopores of SiMPs can result in a boost in their longitudinal relaxivity. Our method is quite general and can be used for any Gd-based CA. We successfully examined the generality of our principle by confining three different Gd-based CAs within SiMPs. Geometrical confinement can reduce the ability of CAs to tumble, decrease the mobility of the water molecules, and

favor clustering and mutual interactions among the loaded CAs, thus altering the original values of the governing parameters q, τ_m,τ_R, and τ_D, and potentially others, as well. The diamagnetic nature of SiMPs suggests that other nanomaterials-based constructs (such as Au NPs) can enhance relaxivity equally effectively. The SiMPs also offer a formidable particle-based system for efficient intravascular delivery. The size, shape, and surface properties of the SiMPs can be rationally designed and tailored for favorable pharmacokinetics and biological targeting.[89-91] Finally, the porous structure of our nanoconstructs can be loaded with multiple agents, such as other nanoparticles and/or small molecules and drugs,[92] to generate highly-multifunctional systems with both imaging and therapeutic capabilities.

FUTURE DIRECTIONS

GNTs as low-field MRI CAs

The longitudinal relaxivities of GNTs as measured in a 0.2 T scanner are the first such measurements of GNTs in a clinical setting. The relaxivity values of GNTs are significantly higher than conventional Gd-chelates at all magnetic field strengths. However, the unusually high relaxivity of GNTs below 10 MHz (Larmor frequency) is unique and difficult to explain using traditional MR relaxation theory. Detailed studies such as temperature dependent NMRD and O-17 NMR studies (to determine the proton exchange rate) are required to understand the low-field behavior of GNTs.

It is also interesting to note that GadoDex exhibits a much higher relaxivity (~ 800 $mM^{-1}s^{-1}$ per Gd^{3+} ion) than Pluronic®-coated GNTs (~350 $mM^{-1}s^{-1}$). This is contrary to the observation at medium-to-high magnetic field strengths (10-100 MHz) where there is no significant difference in relaxivity between GadoDex and Pluronic®-coated GNTs (~ 70 $mM^{-1}s^{-1}$at 1.41 T). The symmetry of the CAs and molecular vibrations are known to produce interesting properties at low-field strengths.[11] One of the observable structural differences between pluronic®-coated GNTs and GadoDex is the mechanism of nanotube suspension. Many of the polymers (including Pluronic®) are known to wrap around the SWNT surface, whereas, carboxylated-dextran suspends the US-tubes only in the presence of Gd^{3+} ions (**Figure 36**). Hence, further experiments are needed to understand the interaction between the Gd^{3+} ions of the GNTs and carboxylated dextran and the impact of these interactions on the symmetry and molecular vibrational properties of GNTs.

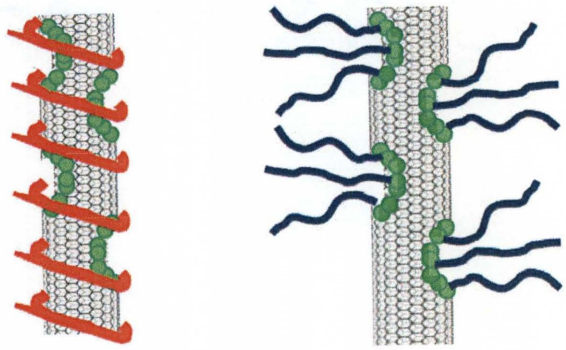

Pluronic wrapped GNTs **GadoDex**

Figure 36. Schematic representations of Pluronic-coated GNTs and GadoDex.

In addition, it has been observed that the intracellular contrast enhancement is highly dependent on the concentration of GNTs within the cell. However, it is probably not correct to attribute the contrast enhancement solely to concentration-based aggregation of GNTs inside the cells. Each cell compartment has unique water exchange properties (which affect the proton relaxation mechanism); however, GNTs of our studies have not been specifically targeted to any sub-cellular compartment. GNTs functionalized to specifically target a cellular compartment would give us an understanding of the effect of sub-cellular localization on the proton relaxation properties. In addition, the threshold [Gd^{3+}] needed for an observable MR signal at low-field strengths needs to be established to enable molecular and cellular MR imaging at low fields.

GadoDex

The biologically benign properties of dextran offer exceptional promise for the use of GadoDex as an intravascular MRI CA and also for advanced applications such as cellular

and molecular imaging. The ease of functionalization of the dextran moiety should help in achieving specific targeting with peptides and/or antibodies. Although, GadoDex exhibited a longitudinal relaxivity (r_1) ca. 25 times greater than clinically-used Gd^{3+}-complexes, the fitting of the nuclear magnetic relaxation dispersion (NMRD) curve indicates that the number of inner-sphere water molecules (q = 2) is not significantly different from conventional Gd-chelates (q = 1-2). This is surprising considering the fact that US-tubes do not interact chemically with Gd^{3+}-ion clusters. Hence, most of the coordination sites of hydrated Gd^{3+} ion (q = 8-9) were expected to be available for proton exchange with bulk water. Some of these coordination sites may be accounted for by the formation of hydroxyl bridges among Gd^{3+} ions in GNTs, and the shielding by the hydrophobic US-tube surface. However, we believe that the dispersion of GadoDex is due to a weak carboxylate (from dextran)-Gd^{3+} interaction (Figure 33). This certainly would decrease the number coordination sites available for proton exchange in GadoDex. One of the possible ways to optimize the relaxivity of GadoDex without affecting the dispersibility is to covalently functionalize the GNT surface with the dextran moiety. In addition, it was also observed that GadoDex lacks solution stability in phosphate-buffered saline (PBS) (visible precipitation of GNTs occurs in 1 hour). This lack of stability will hinder the development of GadoDex for imaging applications that require prolonged blood circulation properties. One of the possible reasons for the lack of stability of GadoDex is the weak coordination bond between Gd^{3+} ions and the carboxylate groups. Thus, covalent functionalization of GNTs with dextran should also assist in the stability of GadoDex under physiological medium.

GNTs and US-tubes as T_2-weighted MRI CAs

GNTs exhibit very-high transverse relaxivities at high magnetic field strengths (≥ 3T). Their lipophilicity and exceptionally large relaxivities have resulted in the first non-iron oxide-based CAs for single-cell imaging. It has been observed that the aggregation of GNTs within the cell plays a pivotal role in the transverse relaxation properties of GNTs. All of our studies were performed with polymer wrapped tubes, which are not targeted. It is also known that the Pluronic® coating is quickly replaced by proteins in physiological medium. This might be the main reason for the observed aggregation of GNTs within the cell. However, for biological applications involving GNTs, covalent functionalization is preferred over non-covalent dispersion of GNTs. In such cases, the aggregation of GNTs will likely be considerably different. Hence, for clinical translation of our *in vitro* and *in vivo* results of GNTs as T_2-weighted MRI CAs, the role of the functionalization (non-covalent vs. covalent) needs to be more thoroughly understood.

The inherent transverse relaxation properties of SWNT materials offer a possible method to track the long-term fate of SWNT-based technologies in biology. Better relaxivities with lower metal catalyst content suggest that the role of the SWNT structure cannot be neglected. However, the non-availability of metal free SWNTs makes this suggestion only a hypothesis. It was observed that, regardless of the synthesis procedure and the nature of metal catalyst particles, the SWNTs are excellent T_2-weighted MRI CAs. However, a comparison between SWNTs produced by different methods could not be achieved in this work due to the lack of complete magnetic characterization of the SWNT materials other than that of HiPco origin. Hence, studies focusing on magnetic characterization of SWNTs should help optimize the T_2-relaxation properties of SWNT materials for all biological applications.

BIBLIOGRAPHY

1. Hinshaw, W. S.; Bottomley, P. A.; Holland, G. N. *Nature* **1977,** 270, (5639), 722-3.

2. Mansfield, P. *Angew. Chem., Int. Ed.* **2004,** 43, (41), 5456-5464.

3. Weissleder, R.; Pittet, M. J. *Nature* **2008,** 452, (7187), 580-589.

4. Sven Mansson, A. B., Physical Principles of Medical Imaging by Nuclear Magnetic Resonance. In *The Chemistry of CAs in Medical Magnetic Resonance Imaging*, Andre Merbach, E. T., Ed. John Wiley & Sons, Ltd: 2001; pp 1-43.

5. Pautler Robia, G. *Physiology* **2004,** 19, 168-75.

6. Lauffer, R. B. *Chem. Rev.* **1987,** 87, (5), 901-27.

7. Eva Toth, L. H., Andre E. Merbach, Relaxivity of Gadolinium (III) Complexes: Theory and Mechanism. In *The Chemistry of CAs in Medical Magnetic Resonance Imaging*, Andre Merbach, E. T., Ed. John Wiley & Sons, Ltd: 2001; pp 45-119.

8. A market summary report for MRI is available at http://www.imvinfo.com/

9. Caravan, P.; Ellison, J. J.; McMurry, T. J.; Lauffer, R. B. *Chem. Rev.* **1999,** 99, (9), 2293-2352.

10. Laurent, S.; Vander Elst, L.; Muller, R. N. *Contrast Media Mol. Imaging* **2006,** 1, (3), 128-137.

11. Toth, E.; Helm, L.; Merbach, A. E., Relaxivity of gadolinium (III) complexes: theory and mechanism. In *Chem. CAs Med. Magn. Reson. Imaging*, 2001; pp 45-119.

12. Nunn, A. D.; Linder, K. E.; Tweedle, M. F. *Q J Nucl Med* **1997,** 41, (2), 155-62.

13. Kroto, H. W.; Heath, J. R.; O'Brien, S. C.; Curl, R. F.; Smalley, R. E. *Nature* **1985,** 318, (6042), 162-3.

14. Bethune, D. S.; Kiang, C. H.; de Vries, M. S.; Gorman, G.; Savoy, R.; Vazquez, J.;

Beyers, R. *Nature* **1993,** 363, (6430), 605-7.

15. Iijima, S.; Ichihashi, T. *Nature* **1993,** 363, (6430), 603-5.
16. Ashcroft, J. M.; Hartman, K. B.; Kissell, K. R.; Mackeyev, Y.; Pheasant, S.; Young, S.; Van der Heide, P. A. W.; Mikos, A. G.; Wilson, L. J. *Adv. Mater.* **2007,** 19, (4), 573-576.
17. Hartman, K. B.; Hamlin, D. K.; Wilbur, D. S.; Wilson, L. J. *Small* **2007,** 3, (9), 1496-1499.
18. Sitharaman, B.; Kissell, K. R.; Hartman, K. B.; Tran, L. A.; Baikalov, A.; Rusakova, I.; Sun, Y.; Khant, H. A.; Ludtke, S. J.; Chiu, W.; Laus, S.; Toth, E.; Helm, L.; Merbach, A. E.; Wilson, L. J. *Chem. Commun.* **2005**, (31), 3915-3917.
19. Perazella, M. A. *Clin. J. Am. Soc. Nephrol.* **2007,** 2, (2), 200-202.
20. Ou, Z.; Wu, B.; Xing, D.; Zhou, F.; Wang, H.; Tang, Y. *Nanotechnology* **2009,** 20, (10), 105102/1-105102/7.
21. Mackeyev, Y.; Hartman, K. B.; Ananta, J. S.; Lee, A. V.; Wilson, L. J. *J. Am. Chem. Soc.* **2009,** 131, (24), 8342-8343.
22. Hayashi, N.; Watanabe, Y.; Masumoto, T.; Mori, H.; Aoki, S.; Ohtomo, K.; Okitsu, O.; Takahashi, T. *Magn Reson Med Sci* **2004,** 3, (1), 27-38.
23. Marti-Bonmati, L.; Kormano, M. *Eur Radiol* **1997,** 7 Suppl 5, 263-8.
24. Peller, M.; Reinl Herbert, M.; Weigel, A.; Meininger, M.; Issels Rolf, D.; Reiser, M. *Magn Reson Med* **2002,** 47, (6), 1194-201.
25. Rooney, W. D.; Johnson, G.; Li, X.; Cohen, E. R.; Kim, S.-G.; Ugurbil, K.; Springer, C. S., Jr. *Magn. Reson. Med.* **2007,** 57, (2), 308-318.
26. Chang, K. H.; Ra, D. G.; Han, M. H.; Cha, S. H.; Kim, H. D.; Han, M. C. *AJNR Am J*

Neuroradiol **1994,** 15, (8), 1413-9; discussion 1420-3.

27. Lindsey, R. O.; Yetkin, F. Z.; Prost, R.; Haughton, V. M. *AJNR Am J Neuroradiol* **1994,** 15, (10), 1849-52.
28. Hasebroock, K. M.; Serkova, N. J. *Expert Opin. Drug Metab. Toxicol.* **2009,** 5, (4), 403-416.
29. Bulte, J. W. M.; Kraitchman, D. L. *NMR Biomed.* **2004,** 17, (7), 484-499.
30. Heyn, C.; Ronald John, A.; Ramadan Soha, S.; Snir Jonatan, A.; Barry Andrea, M.; MacKenzie Lisa, T.; Mikulis David, J.; Palmieri, D.; Bronder Julie, L.; Steeg Patricia, S.; Yoneda, T.; MacDonald Ian, C.; Chambers Ann, F.; Rutt Brian, K.; Foster Paula, J. *Magn Reson Med* **2006,** 56, (5), 1001-10.
31. Gu, Z.; Peng, H.; Hauge, R. H.; Smalley, R. E.; Margrave, J. L. *Nano Lett.* **2002,** 2, (9), 1009-1013.
32. Merbach, A. E.; Toth, E.; Editors, *The Chemistry of CAs in Medical Magnetic Resonance Imaging*. 2001; p 471 pp.
33. Billotey, C.; Wilhelm, C.; Devaud, M.; Bacri, J. C.; Bittoun, J.; Gazeau, F. *Magn. Reson. Med.* **2003,** 49, (4), 646-654.
34. Kuhlpeter, R.; Dahnke, H.; Matuszewski, L.; Persigehl, T.; von Wallbrunn, A.; Allkemper, T.; Heindel Walter, L.; Schaeffter, T.; Bremer, C. *Radiology* **2007,** 245, (2), 449-57.
35. Simon Gerhard, H.; Bauer, J.; Saborovski, O.; Fu, Y.; Corot, C.; Wendland Michael, F.; Daldrup-Link Heike, E. *Eur Radiol* **2006,** 16, (3), 738-45.
36. Hartman, K. B.; Laus, S.; Bolskar, R. D.; Muthupillai, R.; Helm, L.; Toth, E.; Merbach, A. E.; Wilson, L. J. *Nano Lett.* **2008,** 8, (2), 415-419.

37. Moore, V. C.; Strano, M. S.; Haroz, E. H.; Hauge, R. H.; Smalley, R. E.; Schmidt, J.; Talmon, Y. *Nano Lett.* **2003,** 3, (10), 1379-1382.

38. Cherukuri, P.; Gannon, C. J.; Leeuw, T. K.; Schmidt, H. K.; Smalley, R. E.; Curley, S. A.; Weisman, R. B. *Proc. Natl. Acad. Sci. U. S. A.* **2006,** 103, (50), 18882-18886.

39. Frazier, R. A.; Matthijs, G.; Davies, M. C.; Roberts, C. J.; Schacht, E.; Tendler, S. J. B. *Biomaterials* **2000,** 21, (9), 957-966.

40. Ostuni, E.; Chapman, R. G.; Holmlin, R. E.; Takayama, S.; Whitesides, G. M. *Langmuir* **2001,** 17, (18), 5605-5620.

41. Mandeville, J. B.; Moore, J.; Chesler, D. A.; Garrido, L.; Weissleder, R.; Weisskoff, R. M. *Magn. Reson. Med.* **1997,** 37, (6), 885-890.

42. Kawaguchi, T.; Hanaichi, T.; Hasegawa, M.; Maruno, S. *J. Mater. Sci.: Mater. Med.* **2001,** 12, (2), 121-127.

43. Barone, P. W.; Strano, M. S. *Angew. Chem., Int. Ed.* **2006,** 45, (48), 8138-8141.

44. Weissleder, R.; Bogdanov, A.; Neuwelt, E. A.; Papisov, M. *Adv. Drug Delivery Rev.* **1995,** 16, (2,3), 321-33.

45. Kruk, D.; Kowalewski, J. *J. Chem. Phys.* **2009,** 130, (17), 174104/1-174104/12.

46. Laus, S.; Sitharaman, B.; Toth, E.; Bolskar, R. D.; Helm, L.; Wilson, L. J.; Merbach, A. E. *J. Phys. Chem. C* **2007,** 111, (15), 5633-5639.

47. Laurent, S.; Forge, D.; Port, M.; Roch, A.; Robic, C.; Vander Elst, L.; Muller, R. N. *Chem. Rev.* **2008,** 108, (6), 2064-2110.

48. Welsher, K.; Liu, Z.; Daranciang, D.; Dai, H. *Nano Lett.* **2008,** 8, (2), 586-590.

49. Liu, Z.; Davis, C.; Cau, W.; He, L.; Chen, X.; Dai, H. *Proc. Natl. Acad. Sci. U. S. A.* **2008,** 105, (5), 1410-1415.

50. Bussy, C.; Cambedouzou, J.; Lanone, S.; Leccia, E.; Heresanu, V.; Pinault, M.; Mayne-l'Hermite, M.; Brun, N.; Mory, C.; Cotte, M.; Doucet, J.; Boczkowski, J.; Launois, P. *Nano Lett.* **2008,** 8, (9), 2659-2663.

51. Kim, B. M.; Qian, S.; Bau, H. H. *Nano Lett.* **2005,** 5, (5), 873-878.

52. Choi, J. H.; Nguyen, F. T.; Barone, P. W.; Heller, D. A.; Moll, A. E.; Patel, D.; Boppart, S. A.; Strano, M. S. *Nano Lett.* **2007,** 7, (4), 861-867.

53. Singh, R.; Pantarotto, D.; Lacerda, L.; Pastorin, G.; Klumpp, C.; Prato, M.; Bianco, A.; Kostarelos, K. *Proc. Natl. Acad. Sci. U. S. A.* **2006,** 103, (9), 3357-3362.

54. Porter, A. E.; Gass, M.; Muller, K.; Skepper, J. N.; Midgley, P. A.; Welland, M. *Nat. Nanotechnol.* **2007,** 2, (11), 713-717.

55. Sitharaman, B.; Van Der Zande, M.; Ananta, J. S.; Shi, X.; Veltien, A.; Walboomers, X. F.; Wilson, L. J.; Mikos, A. G.; Heerschap, A.; Jansen, J. A. *J. Biomed. Mater. Res., Part A* 93A, (4), 1454-1462.

56. Haacke, E. M.; Xu, Y.; Cheng Yu-Chung, N.; Reichenbach Jurgen, R. *Magn Reson Med* **2004,** 52, (3), 612-8.

57. Hassan, A. A.; Chan, B. T.-Y.; Tran, L. A.; Hartman, K. B.; Ananta, J. S.; Mackeyev, Y.; Hu, L.; Pautler, R. G.; Wilson, L. J.; Lee, A. V. *Contrast Media Mol. Imaging* 5, (1), 34-38.

58. Terreno, E.; Crich, S. G.; Belfiore, S.; Biancone, L.; Cabella, C.; Esposito, G.; Manazza, A. D.; Aime, S. *Magn. Reson. Med.* **2006,** 55, (3), 491-497.

59. Frangioni John, V.; Hajjar Roger, J. *Circulation* **2004,** 110, (21), 3378-83.

60. Shapiro, E. M.; Medford-Davis, L. N.; Fahmy, T. M.; Dunbar, C. E.; Koretsky, A. P. *Contrast Media Mol. Imaging* **2007,** 2, (3), 147-153.

61. Shapiro, E. M.; Skrtic, S.; Sharer, K.; Hill, J. M.; Dunbar, C. E.; Koretsky, A. P. *Proc. Natl. Acad. Sci. U. S. A.* **2004,** 101, (30), 10901-10906.

62. Anderson Stasia, A.; Lee Kristen, K.; Frank Joseph, A. *Invest Radiol* **2006,** 41, (3), 332-8.

63. Patra, C. R.; Bhattacharya, R.; Mukherjee, P. *J. Mater. Chem.* 20, (3), 547-554.

64. Tasciotti, E.; Liu, X.; Bhavane, R.; Plant, K.; Leonard, A. D.; Price, B. K.; Cheng, M. M.-C.; Decuzzi, P.; Tour, J. M.; Robertson, F.; Ferrari, M. *Nat. Nanotechnol.* **2008,** 3, (3), 151-157.

65. Tripisciano, C.; Kraemer, K.; Taylor, A.; Borowiak-Palen, E. *Chem. Phys. Lett.* **2009,** 478, (4-6), 200-205.

66. Tong, L.; Wei, Q.; Wei, A.; Cheng, J.-X. *Photochem. Photobiol.* **2009,** 85, (1), 21-32.

67. Heinrich, J. L.; Curtis, C. L.; Credo, G. M.; Kavanagh, K. L.; Sailor, M. J. *Science,* **1992,** 255, (5040), 66-8.

68. Mackeyev, Y.; Bachilo, S.; Hartman, K. B.; Wilson, L. J. *Carbon* **2007,** 45, (5), 1013-1017.

69. Al Faraj, A.; Cieslar, K.; Lacroix, G.; Gaillard, S.; Canet-Soulas, E.; Cremillieux, Y. *Nano Lett.* **2009,** 9, (3), 1023-1027.

70. Liu, X.; Guo, L.; Morris, D.; Kane, A. B.; Hurt, R. H. *Carbon* **2008,** 46, (3), 489-500.

71. Ruggiero, A.; Villa, C. H.; Bander, E.; Rey, D. A.; Bergkvist, M.; Batt, C. A.; Manova-Todorova, K.; Deen, W. M.; Scheinberg, D. A.; McDevitt, M. R. *Proc. Natl. Acad. Sci. U. S. A.* 107, (27), 12369-12374, S12369/1-S12369/7.

72. Zhu, A.; Yuan, L.; Dai, S. *J. Phys. Chem. C* **2008,** 112, (14), 5432-5438.

73. Xi, G.; Wang, C.; Wang, X. *Eur. J. Inorg. Chem.* **2008,** (3), 425-431.

74. Nordblad, P. *Braz. J. Phys.* **2000,** 30, (4), 762-765.

75. Wen, J. Z.; Richter, H.; Green, W. H.; Howard, J. B.; Treska, M.; Jardim, P. M.; Vander Sande, J. B. *J. Mater. Chem.* **2008,** 18, (13), 1561-1569.

76. Kumar, D.; Narayan, J.; Kvit, A. V.; Sharma, A. K.; Sankar, J. *J. Magn. Magn. Mater.* **2001,** 232, (3), 161-167.

77. Chouly, C.; Pouliquen, D.; Lucet, I.; Jeune, J. J.; Jallet, P. *J. Microencapsulation* **1996,** 13, (3), 245-255.

78. Chen, R. B.; Lu, B. J.; Tsai, C. C.; Chang, C. P.; Shyu, F. L.; Lin, M. F. *Carbon* **2004,** 42, (14), 2873-2878.

79. Hod, O.; Barone, V.; Peralta, J. E.; Scuseria, G. E. *Nano Lett.* **2007,** 7, (8), 2295-2299.

80. Chiappini, C.; Tasciotti, E.; Fakhoury Jean, R.; Fine, D.; Pullan, L.; Wang, Y.-C.; Fu, L.; Liu, X.; Ferrari, M. *Chemphyschem* 11, (5), 1029-35.

81. Toth, E.; Bolskar, R. D.; Borel, A.; Gonzalez, G.; Helm, L.; Merbach, A. E.; Sitharaman, B.; Wilson, L. J. *J. Am. Chem. Soc.* **2005,** 127, (2), 799-805.

82. Li, Z.; Drazer, G. *Phys. Fluids* **2006,** 18, (11), 117102/1-117102/7.

83. Strijkers, G. J.; Mulder, W. J. M.; van Heeswijk, R. B.; Frederik, P. M.; Bomans, P.; Magusin, P. C. M. M.; Nicolay, K. *Magn. Reson. Mater. Phys., Biol. Med.* **2005,** 18, (4), 186-192.

84. Talanov, V. S.; Regino, C. A. S.; Kobayashi, H.; Bernardo, M.; Choyke, P. L.; Brechbiel, M. W. *Nano Lett.* **2006,** 6, (7), 1459-1463.

85. Avedano, S.; Tei, L.; Lombardi, A.; Giovenzana, G. B.; Aime, S.; Longo, D.; Botta, M. *Chem. Commun. (Cambridge, U. K.)* **2007**, (45), 4726-4728.

86. Yang, J. J.; Yang, J.; Wei, L.; Zurkiya, O.; Yang, W.; Li, S.; Zou, J.; Zhou, Y.; Maniccia, A. L. W.; Mao, H.; Zhao, F.; Malchow, R.; Zhao, S.; Johnson, J.; Hu, X.; Krogstad, E.; Liu, Z.-R. *J. Am. Chem. Soc.* **2008,** 130, (29), 9260-9267.

87. Laus, S.; Sitharaman, B.; Toth, E.; Bolskar, R. D.; Helm, L.; Asokan, S.; Wong, M. S.; Wilson, L. J.; Merbach, A. E. *J. Am. Chem. Soc.* **2005,** 127, (26), 9368-9369.

88. Botta, M. *Eur. J. Inorg. Chem.* **2000**, (3), 399-407.

89. Decuzzi, P.; Ferrari, M. *Biomaterials* **2006,** 27, (30), 5307-5314.

90. Decuzzi, P.; Pasqualini, R.; Arap, W.; Ferrari, M. *Pharm. Res.* **2009,** 26, (1), 235-243.

91. Decuzzi, P.; Godin, B.; Tanaka, T.; Lee, S. Y.; Chiappini, C.; Liu, X.; Ferrari, M. *J. Controlled Release* 141, (3), 320-327.

92. Tanaka, T.; Mangala, L. S.; Vivas-Mejia, P. E.; Nieves-Alicea, R.; Mann, A. P.; Mora, E.; Han, H.-D.; Shahzad, M. M. K.; Liu, X.; Bhavane, R.; Gu, J.; Fakhoury, J. R.; Chiappini, C.; Lu, C.; Matsuo, K.; Godin, B.; Stone, R. L.; Nick, A. M.; Lopez-Berestein, G.; Sood, A. K.; Ferrari, M. *Cancer Res.* 70, (9), 3687-3696.